nature communications

Article

https://doi.org/10.1038/s41467-025-59526-3

Nucleoporins shape germ granule architecture and balance small RNA silencing pathways

Received: 25 July 2024

Accepted: 24 April 2025

Published online: 08 May 2025

Check for updates

Kun Shi[1,3], Ying Zhang[1,3], Zhenzhen Du[1], Symonne C. Liu[2], Ivan Leon[2], Xinyu Fan[1], Heng-Chi Lee[2] & Donglei Zhang[2]

Animals use small RNA pathways, such as PIWI-interacting RNA (piRNA) and small interfering RNA (siRNA), to silence harmful genetic elements. In *Caenorhabditis elegans*, piRNA pathway components are organized into sub-compartments within germ granules near nuclear pore complexes, but the basis and function of this association have remained unclear. Here, our data suggest that germ granule formation and nuclear pore clustering are interdependent processes. We identify the conserved nucleoporins NPP-14/NUP214 and NPP-24/NUP88, along with the germ granule protein EPS-1, as key factors anchoring germ granules to nuclear pores. Loss of these factors leads to disorganized, fused granules and enhanced piRNA silencing. Artificial tethering of granule sub-compartments mimics this effect. However, this increase in piRNA silencing comes at the expense of RNA interference efficiency and heritability. Our findings reveal the molecular factors mediating germ granule–nuclear pore interaction and highlight how spatial organization of RNA silencing machinery fine-tunes gene regulation.

Small RNA pathways play crucial roles in genome defense by silencing invasive nucleic acids such as transposons and viruses[1]. Among these pathways, PIWI-interacting RNAs (piRNAs) and small interfering RNAs (siRNAs) have been extensively studied for their involvement in safeguarding genome integrity[2]. In the nematode *Caenorhabditis elegans* (*C. elegans*), both piRNA and siRNA pathways operate in the defense against transposable elements[3] and share common downstream components[4,5], suggesting potential crosstalk and coordinated regulation between them. Indeed, in PIWI *prg-1* mutant, which lacks all piRNAs, the duration of RNAi (siRNA) inheritance is enhanced[6]. However, whether there is a regulatory mechanism controlling the efficacy of piRNAs is not known.

Central to piRNA-mediated gene regulation is the organization of the piRNA pathway factors within specialized cytoplasmic structures known as germ granules[7]. These membrane-less organelles serve as hubs for RNA metabolism and regulation in the germline[8]. Germ granules exhibit a remarkable organization into distinct sub-compartments, including P granules, Z granules, SIMR foci, D granule, E granule, and mutator foci, each with specific molecular factors involved in distinct steps of small RNA silencing[9–14]. These observations suggest that distinct germ granule sub-compartments may coordinate to ensure proper initiation and amplification of gene silencing signals.

Germ granules have been observed to be closely associated with nuclear pores in various animals, including zebrafishes, worms, flies, and mice[15–18]. In *C. elegans* germline, germ granules are shown to be the extensions of nuclear pore complexes (NPCs) and serve as major sites for RNA export[19,20]. In addition, nuclear pores have been reported to be clustered in the germline of worms, mice, guinea pigs, and human[20–22]. Despite the association between germ granules and NPCs have been reported for decades, several key questions remain unanswered; what are the factors mediating germ granule and NPC interactions? How are nuclear pores clustered in the germline? In addition, what is the

[1]Department of Biochemistry and Molecular Biology, School of Basic Medicine, Tongji Medical College, Huazhong University of Science and Technology, Wuhan, Hubei 430032, China. [2]Department of Molecular Genetics and Cell Biology, University of Chicago, Chicago, IL 60637, USA. [3]These authors contributed equally: Kun Shi, Ying Zhang. e-mail: hengchilee@uchicago.edu; dlzhang@uchicago.edu

functional significance of germ granule and NPC interaction in small RNA-mediated silencing? Previous studies examining the contribution of NPC factor nucleoporins in germ granule assembly focus on analyzing the early embryos of *C. elegans*[23,24]. Nonetheless, as several of the key piRNA factors are only enriched in the germ granule in the adult germline but not in the early embryo[25,26], analyses are needed to examine the germ granule-NPC association in the adult germline as well in order to investigate their potential roles in small RNA gene silencing.

Results

Nucleoporin NPP-14 (NUP214) and NPP-24 (NUP88) negatively regulate piRNA silencing

In our previous investigations, we utilized GFP-based piRNA reporters to identify factors that positively regulate piRNA-mediated gene silencing[27,28]. Our previous observations indicated that knockdown of certain nucleoporins (NPPs) appeared to slightly increase the percentage of piRNA reporter-silenced animals. However, due to the variability in silencing among wild-type animals, these small changes were not statistically significant[27]. We noticed that for another piRNA reporter, the GFP-targeting piRNA effectively silences GFP expression at 20 °C[29], yet such silencing efficacy diminishes at 25 °C (Fig. 1a), likely attributable to reduced piRNA expression levels at the elevated temperature[30]. To identify the negative regulators of piRNA silencing, we conducted a targeted RNAi screen of selected NPPs, focusing primarily on those located on the cytoplasmic side of nuclear pores that may interact with germ granules (Fig. S1a), to assess their impact on the piRNA reporter silencing under the elevated temperature where reporter silencing is compromised. Our screening revealed that RNAi targeting a few nucleoporin genes, including *npp-14, npp-9, npp-17*, and *npp-24*, significantly increased the proportion of animals exhibiting gene silencing of the piRNA reporter at 25 °C (Fig. S1b, c). Since *npp-17* knockdown reduced GFP reporter expression even in the absence of GFP-targeting piRNA (Fig. S1b), its effect on the piRNA reporter is likely independent of the piRNA pathway. Additionally, *npp-9* RNAi only mildly enhanced piRNA silencing and did not produce a clear P granule phenotype (see details below). Therefore, neither *npp-17* nor *npp-9* were further investigated in this study. We further corroborate the roles of *npp-14* and *npp-24* in piRNA silencing using null mutants created by CRISPR-Cas9 (Fig. 1b and S1d). NPP-14 and NPP-24 are homologs of human NUP214 and NUP88, respectively, which are known to localize at the cytoplasmic filaments of NPC (Fig. 1c)[31]. Given that both the *npp-14(dz7)* and the *npp-24(dz12)* null mutants exhibited normal viability with a brood size comparable to that of the wildtype (Fig. S1e), it indicates that the overall functionality of NPCs remains intact in the absence of NPP-14 or NPP-24. To ascertain whether the silencing of the GFP piRNA reporter in *npp-14* is contingent upon piRNA activity, we knock-outed the PIWI Argonaute gene *prg-1*, followed by *npp-14*, in the piRNA reporter strain (Fig. 1d). We observed that these *npp-14* mutant animals do not trigger gene silencing of GFP reporter in the absence of *prg-1* (Fig. 1e), indicating that NPP-14 contribute to GFP reporter silencing in a piRNA-dependent manner. Conversely, when *npp-14* was knocked out prior to *prg-1*, the piRNA reporter remained silenced for at least 5 generations (Fig. 1d, e). It is known that piRNA silencing, once established, can be maintained without piRNAs for generations[32,33]. This finding suggests that once established, the silencing state of the piRNA reporter can be maintained independently of piRNA in this *npp-14* mutant. Collectively, our candidate RNAi screen unveiled NPP-14 and NPP-24 nucleoporins as negative regulators of piRNA reporter silencing under elevated temperature.

NPP-14 and NPP-24 promote germ granules–NPC interactions

As mentioned above, previous studies have demonstrated that germ granules assemble at NPC clusters in the germline[16,19]. In addition, disruption of P granules compromises piRNA silencing[34,35]. Given our findings of the regulatory roles of NPP-14 and NPP-24 in piRNA silencing, we investigated whether NPP-14 and NPP-24 regulate the assembly of germ granules and NPC clustering. Our observations support the role of NPP-14 and NPP-24 in mediating NPC interaction with germ granules. First, we observed the morphology of mRuby::PGL-1 (a P granule marker) changed from an extended oval shape to a rounded shape, indicating a loss of stable anchoring in the *npp-14(dz7)* or in the *npp-24(dz12)* mutant (Fig. 2a). Second, while mRuby::PGL-1 foci are exclusively associated with the nucleus in the syncytial cytoplasm in the wild-type animals, these foci were also observed in the syncytial cytoplasm in the *npp-14(dz7)* mutant or *npp-24(dz12)* mutant (Fig. 2b), further supporting the notion that germ granules are no longer stably anchored to the NPC. Third, time-lapse live imaging revealed fusion events of PGL-1::GFP foci at the nuclear periphery in *npp-14(dz7)* animals (Fig. S2a). This fusion event likely results from a weakened interaction with NPC, increasing germ granule mobility and facilitating fusion. Fourth, likely due to germ granule fusion, fewer but larger perinuclear mRuby::PGL-1 foci were observed in the *npp-14(dz7)* or in the *npp-24(dz12)* mutant (Fig. 2a, b). The number of PGL-1 foci were also reduced in *npp-14* RNAi but not in *npp-9* or *npp-17* RNAi-treated animals (Fig. S2b). Fewer but larger foci of other germ granule markers, such as GFP::PRG-1 (a P/Z granule marker)[14] and mCherry GLH-1 (a P granule marker), were also observed in the *npp-14(dz7)* or in the *npp-24(dz12)* mutant (Fig. S2c). Immunostaining of endogenous PRG-1 also showed an enlarged PRG-1 foci in the *npp-14(dz7)* mutant (Fig. S2d) and the protein levels of GFP::PRG-1 or PGL-1::GFP did not change in the *npp-14(dz7)* mutant (Fig. S2e). While our imaging assays were conducted with worms grown at 20 °C, fewer but larger GFP::PRG-1 and mCherry::GLH-1 foci were also observed in worms grown at 25 °C (Fig. S2f). Collectively, these observations suggest a weakened association of germ granules with the NPC in the *npp-14* and in the *npp-24* mutants, resulting in changes in germ granules' shape, fusion, and their detachment from the nuclear periphery.

Germ granule–NPC interactions promote NPC clustering and tethering of cytoplasmic nucleoporins

In the *C. elegans* germline, nuclear pores are not randomly distributed but form clusters under germ granules[16]. As germ granules are positioned above nuclear pore clusters (Fig. 2a), we wondered whether NPC clustering might be affected in the *npp-14* or *npp-24* mutants, where perinuclear germ granule anchoring is compromised. Interestingly, in the *npp-14(dz7)* or in the *npp-24(dz12)* mutant, we observed a reduction in the size but an increase in the number of GFP::NPP-9 foci at the nuclear envelope (Fig. 3a, b). Smaller but more numerous NPP-11::RFP foci and GFP::NPP-22 foci were also found in *npp-14(dz7)* mutant (Fig. S3a, b). Nonetheless, the signals of mCherry::NPP7 and mCherry::NPP-1 on the nuclear envelope appeared more diffused and less distinctly clustered, making it challenging to determine whether NPP-14 or NPP-24 influences their clustering (Fig. S3c, d). Collectively, these results suggest that NPC clustering is compromised in the *npp-14* and *npp-24* mutants.

We noticed that NPP-14 and NPP-24 are mutually required for each other's abundance in the adult germline as well as in the late embryos (Fig. 3a–d and Fig. S3e–g), but not in 2 or 4-cell embryos (Fig. S3e). Since it was demonstrated that NPP-14 and NPP-24 homologs directly interact with each other[36,37], it is likely their interactions are critical for their protein stabilities. In contrast, the abundance of other nucleoporins, such as GFP::NPP-9, mCherry::NPP-11, GFP::NPP-22, and mCherry::NPP-1, were not affected in the germ cells of *npp-14(dz7)* or the *npp-24(dz12)* mutant (Fig. 3a–d and S3a–c).

Furthermore, while GFP::NPP-9 foci, NPP-14, and NPP-24 are exclusively associated with the nucleus in the wild-type animals, a fraction of these foci was detected in the germline syncytial cytoplasm in *npp-14(dz7)* and *npp-24(dz12)* mutants (Fig. 3c, d), indicating that NPP-14 and NPP-24 promote the tethering of these cytoplasmic

https://doi.org/10.1038/s41467-025-59526-3

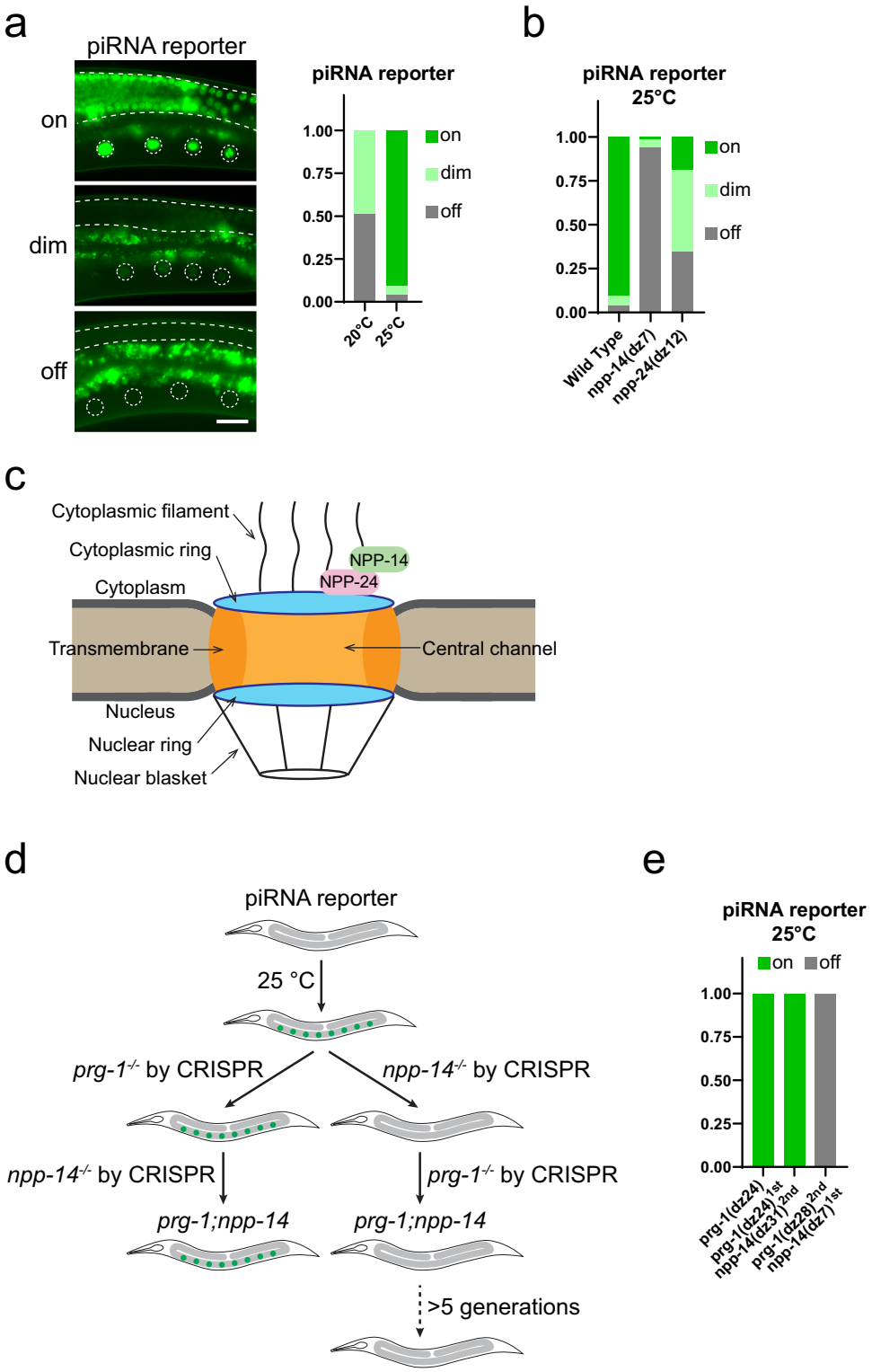

Fig. 1 | NPP-14 and NPP-24 negatively regulate piRNA silencing. a Left: Representative fluorescent micrographs of the piRNA reporter showing different GFP expression levels. In this reporter, the 3′ UTR sequences of *gfp::his-58* are targeted by the endogenous piRNA 21ur-1. Dashed lines and circles denote the germline and maturing oocyte nuclei, respectively. Note that the bright signals observed outside of dashed areas are autofluorescence signals originating from gut granules. Bars: 10 μm. Right: Percentage of screened animals displaying the indicated GFP expression levels of the piRNA reporter for worms grown at the indicated temperature. **b** Percentage of animals screened displaying the indicated levels of GFP expression levels of the piRNA reporter in the indicated strains grown at 25 °C. **c** A schematic illustrating the structure of the nuclear pore complex, highlighting NPP-14 (NUP214 homolog) and NPP-24 (NUP88 homolog) as nucleoporins located at the cytoplasmic filament. **d** A schematic illustrating the piRNA reporter assays used to determine whether the initiation or maintenance of reporter silencing in the *npp-14* mutant requires PIWI PRG-1. **e** Percentage of animals screened displaying the indicated GFP expression levels of the piRNA reporter in the indicated strains grown at 25 °C. *prg-1* and *npp-14* were sequentially knocked out by CRISPR-Cas9 editing, and the order of knockout was indicated.

https://doi.org/10.1038/s41467-025-59526-3

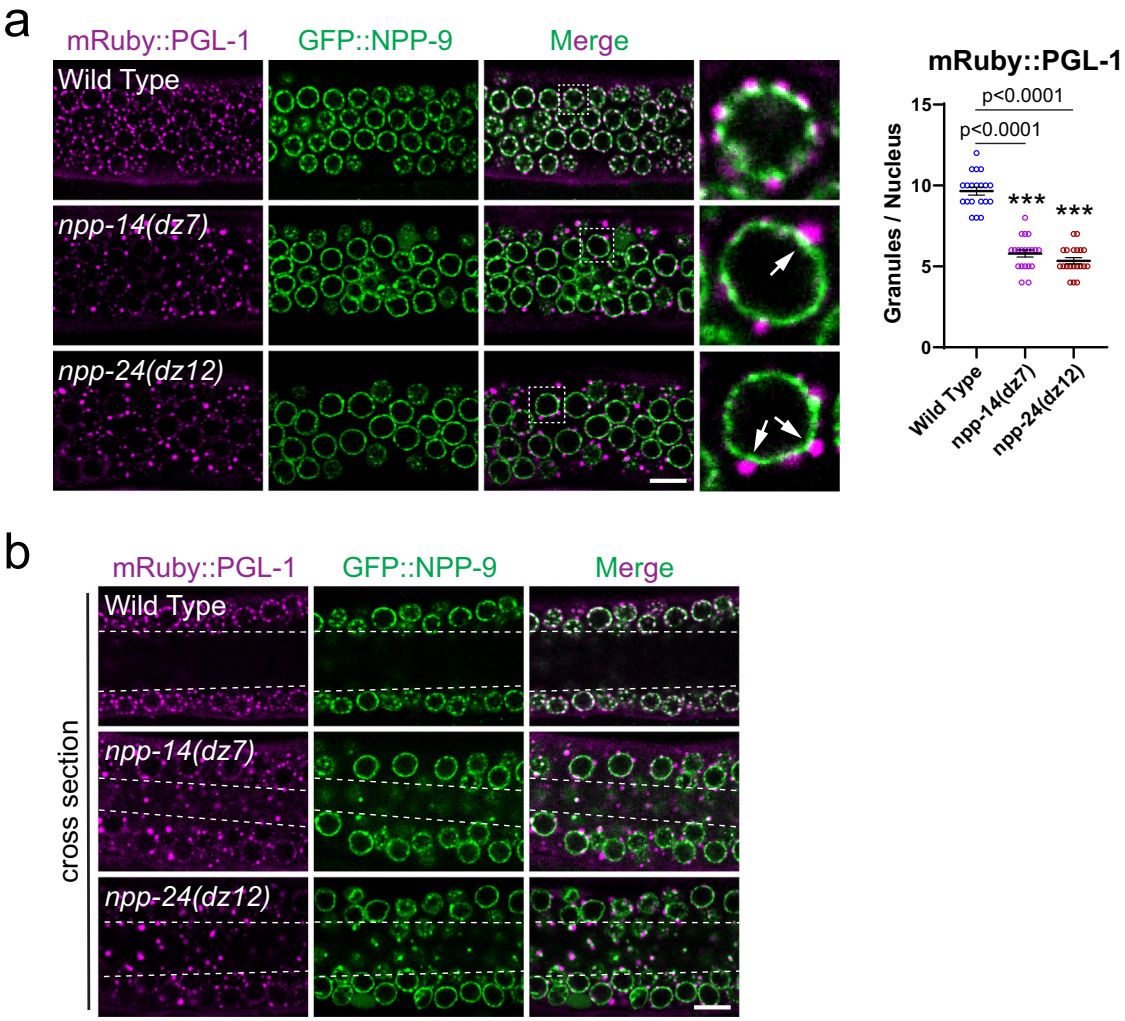

Fig. 2 | Fewer but enlarged germ granules are found in the *npp-14* or *npp-24* mutants. a Fluorescent micrographs showing the localization of mRuby::PGL-1 and GFP::NPP-9 at the germline nuclei from the pachytene region in the indicated strains. Arrows indicate enlarged germ granules. Bars: 10 μm. Right: mean number of granules per nucleus was analyzed using one-way ANOVA, followed by Dunnett's correction for multiple comparisons. Bars indicate the mean. Error bars indicate the standard error mean. $n = 20$. **b** Fluorescent micrographs of the germline cross-section showing the localization of mRuby::PGL-1 and GFP::NPP-9 in the indicated strains. The area between the two dashed lines is germline syncytial cytoplasm. Bars: 10 μm.

nucleoporins to the NPCs. In contrast, central channel nucleoporins, such as mCherry::NPP-1 or NPP-11::RFP, the transmembrane nucleoporin GFP::NPP-22, or nuclear basket nucleoporin mCherry::NPP-7 remained exclusively associated with the nucleus in the *npp-14* mutant (Fig. S3h). Together, these results indicate that NPP-14 and NPP-24 contribute to both the NPC clustering as well as the tethering of some cytoplasmic nucleoporins to NPC in the germline.

While our analyses suggest that NPP-14 and NPP-24 promote the nuclear tethering of germ granules and some cytoplasmic nucleoporin, why are NPC clusters smaller in the *npp-14* or *npp-24* mutant? One possibility is that perinuclear germ granule interactions with NPC contribute to NPC clustering. In this model, the presence of fewer and rounder germ granules may limit their interactions with the NPC, leading to compromised and smaller NPC clusters. If this is the case, we would expect that other mutants affecting perinuclear germ granule formation would also impact NPC clustering. Indeed, in the *mip-1(uae1)* mutant or *mip-1;mip-2 (uae1;uae2)* mutant—where perinuclear P granule formation is partially or severely disrupted[38,39], respectively—we observed that nuclear pore clustering is partially or severely compromised, respectively (Fig. S3i). These observations suggest that perinuclear germ granule–NPC interaction contributes to NPC clustering in the germline.

Proximity labeling identifies EPS-1 as a D granule factor that attenuates piRNA silencing

Our observation that NPP-14 and NPP-24 contribute to the nuclear tethering of germ granules prompted us to identify germ granule factors involved in the interactions between NPCs and P granules. Therefore, we applied TurboID[39] to identify interactors of NPP-14 and PRG-1, components of NPC and P/Z granule, respectively. TurboID is a proximity labeling technique, where TurboID-tagged protein catalyzes the attachment of biotin to nearby proteins within a defined radius. Subsequent streptavidin-affinity purification and mass spectrometry were used for protein identification[39]. We compared streptavidin-enriched biotinylated proteins in the strain expressing TurboID::NPP-14 with those in the control strain expressing only cytoplasmic TurboID. Using criteria of fourfold enrichment and a p value <0.05, we identified 184 proteins significantly enriched by TurboID::NPP-14 labeling (Fig. 4a and Supplementary Data 1). Among these proteins, more than twenty NPC subunits were identified, underscoring the effectiveness of our TurboID-based proteomic analysis (Fig. 4a). Similarly, we identified 122 proteins significantly enriched in the TurboID::PRG-1 expressing strain (Fig. 4a and Supplementary Data 1), among which 11 are known P granule proteins. Principal component analysis (PCA) shows that replicates of different strains cluster together, showing the similarity between repeat samples

https://doi.org/10.1038/s41467-025-59526-3

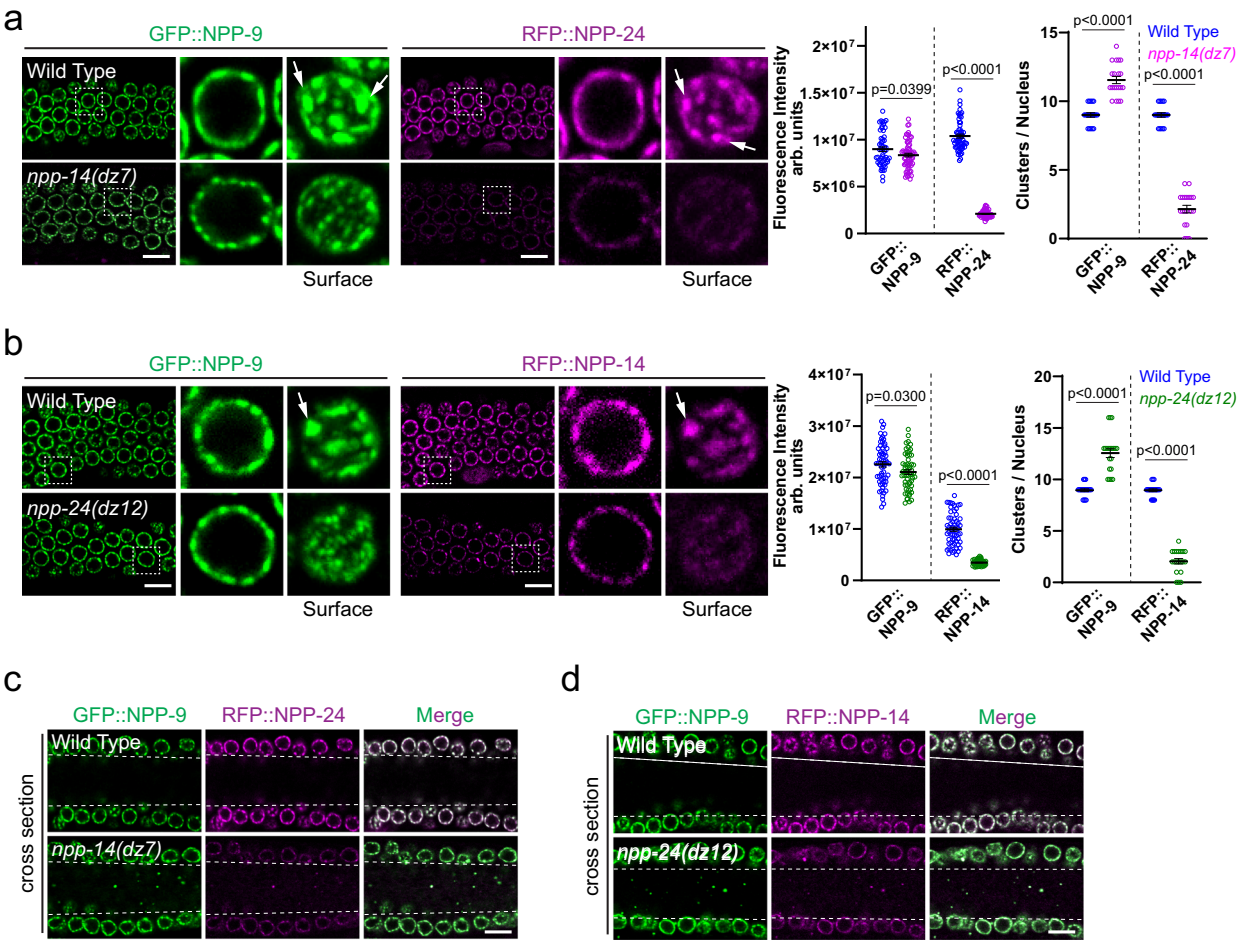

Fig. 3 | NPP-14 and NPP-24 contribute to NPC clustering and are mutually required for their abundance. a, **b** Fluorescent micrographs showing the clustering and expression levels of GFP::NPP-9 and **a** tagRFP::NPP-24 or **b** tagRFP::NPP-14 in the indicated strains. The surface sections of germline nuclei from the pachytene region are shown. Arrows indicate NPC clusters. Bars: 10 μm. Right: fluorescent intensity of clusters ($n = 100$) or mean number of clusters per nucleus ($n = 20$) was analyzed using one-tailed Student's *t*-test. Bars indicate the mean. Errors bars indicate the standard error mean. **c**, **d** Fluorescent micrographs of the germline cross-section showing the localization of GFP::NPP-9 and **c** tagRFP::NPP-24 or **d** tagRFP::NPP-14 in the indicated strains. The area between the two dashed lines is germline syncytial cytoplasm. Bars: 10 μm.

(Fig. S4a). Intriguingly, we found 29 proteins enriched in both TurboID::NPP-14 and TurboID::PRG-1 analyses (Fig. 4b). To determine whether these factors play a role in regulating germ granule formation, we conducted a candidate RNAi screen for many of these genes (Fig. S4b). We discovered that knockdown of *mip-1*, *ddx-19*, or *f56c9.6* resulted in decreased number of perinuclear PRG-1 foci (Fig. 4c). MIP-1/EGGD-1 is a LOTUS domain-containing P granule protein known to promote the assembly and tethering of P granules[38,39], while DDX-19 is an RNA helicase recently identified as a component of D granules[14,20]. F56C9.6 is an uncharacterized protein that has previously been found to associate with P granule factors[39,40]. We further examined whether *mip-1*, *ddx-19*, *f56C9.6*, and most of the interactors shared between NPP-14 and PRG-1 contribute to piRNA reporter silencing. Using RNAi and/or the null mutants generated via CRISPR-Cas9-editing, we found that only *f56c9.6* null mutant resulted in a significant enhancement of piRNA reporter silencing (Fig. 4d and Fig. S4b, c). We designated the *f56c9.6* gene as *eps-1* (enhanced piRNA silencing-1) due to its mutant *eps-1(dz35)* phenotype. The interactions between EPS-1 and NPP-14, PRG-1, or MIP-1 are further confirmed by crosslinked and co-immunoprecipitation[28] analyses (Fig. S4d–f).

To examine the localization of EPS-1, we generated a strain expressing PGL-1::mCardinal, RFP::EPS-1, and GFP::NPP-9. Interestingly, RFP::EPS-1 granules localize between P granules and NPCs (Fig. 4e), implying EPS-1 is located in D granule, a sub-compartment of germ granule that situates between P granule and NPC[14] (Fig. S4g). Indeed, we found that EPS-1 co-localize with CSR-1 and DDX-19, both D granule-enriched factors (Fig. 4f, g)[14]. Notably, we found that the perinuclear localization of DDX-19 and CSR-1 is reduced in the *npp-14(dz7)* mutant and in the *eps-1(dz35)* mutant (Fig. 4f–i and Fig. S4h, i).

EPS-1 promotes germ granule–NPC interactions

If EPS-1 contributes to the germ granule–NPC interaction, we would expect the *eps-1* mutant to exhibit similar germ granule and NPC clustering phenotypes as the *npp-14* mutant. Indeed, we observed fewer but larger PGL-1 germ granules are observed in the *eps-1(dz35)* mutant (Fig. 5a). Additionally, the *eps-1* mutant exhibited smaller, more numerous NPP-9 and NPP-22 foci (Fig. 5b and Fig. S5a), indicating defects in NPC clustering. However, we did not observe PGL-1::GFP foci in the syncytial cytoplasm of the *eps-1(dz35)* mutant (Fig. 5a), suggesting that other germ granule factors also contribute to anchoring germ granules at NPC clusters.

We then investigated the factors required for EPS-1 perinuclear localization. In *npp-14(dz7)* mutants, both the perinuclear accumulation and overall protein levels of RFP::EPS-1 were reduced, whereas they remained unchanged in *mip-1(dz17)* mutants (Figs. 5c and S5b). In contrast, the number of MIP-1::RFP foci, like other P granule proteins, was reduced in both *eps-1(dz35)* and *npp-14(dz7)* mutants (Fig. 5d), despite the overall protein levels of MIP-1::RFP remaining unchanged in either

https://doi.org/10.1038/s41467-025-59526-3

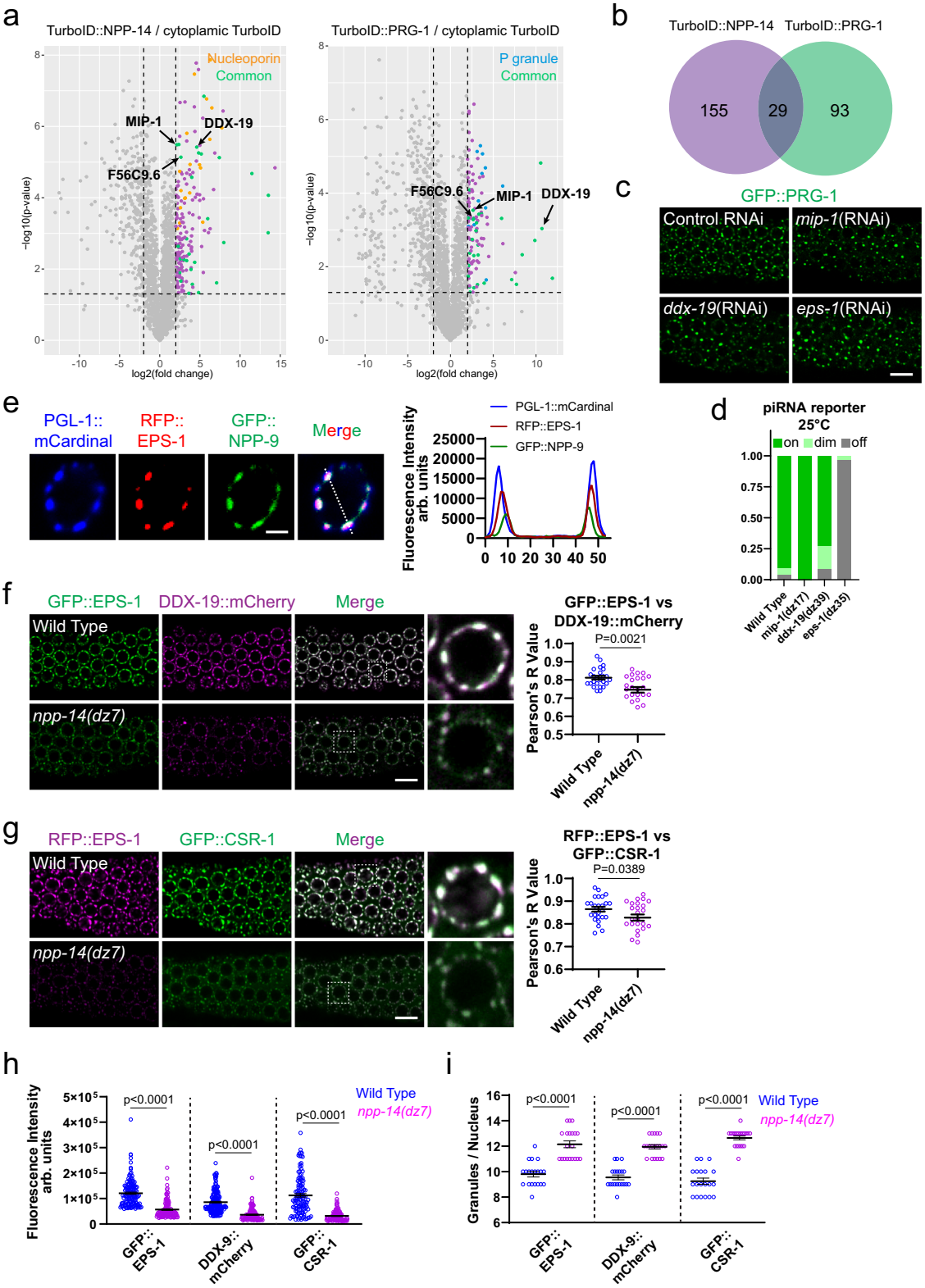

strain (Fig. S5c). These findings suggest that NPP-14 is required for both the perinuclear localization and stability of EPS-1, while both NPP-14 and EPS-1 regulate the perinuclear localization of the P granule factor MIP-1.

To further examine EPS-1's role in NPC–germ granule interactions, we performed crosslinking and co-immunoprecipitation assays. While NPP-14 was co-immunoprecipitated with MIP-1 (a p granule-enriched factor) in the wild-type background, the levels of NPP-14 co-immunoprecipitated with MIP-1 were significantly reduced in the *eps-1(dz35)* mutant (Fig. 5e), supporting that EPS-1 promotes NPP-14 and MIP-1 interactions. Collectively, our data identify EPS-1 as a D granule factor that promotes germ granule–NPC interaction.

NPP-14, NPP-24, and EPS-1 negatively regulate the production of downstream small RNAs from piRNA targeting sites

piRNAs trigger gene silencing by inducing the production of secondary small RNA, known as WAGO 22G-RNA, to promote gene silencing[5]. To

Fig. 4 | Proximity labeling-mass spectrometry analyses identify EPS-1 as a germ granule factor that negatively regulates piRNA silencing. a Volcano plots display the enriched proteins from strains expressing TurboID::NPP-14 and TurboID::PRG-1. Nucleoporins enriched in TurboID::NPP-14 are denoted as orange dots, P granule factors enriched in TurboID::PRG-1 are denoted as blue dots, and proteins enriched in both experiments are depicted as green dots. Statistical significance criteria are log2(Fold change) >2 and $p < 0.05$. **b** A Venn diagram showing the overlap between the enriched proteins from strains expressing TurboID::NPP-14 and TurboID::PRG-1. **c** Fluorescent micrographs showing the localization of GFP::PRG-1 in the indicated RNAi strains. L4440 empty vector was utilized as the RNAi control. Bars: 10 μm. **d** Percentage of screened animals showing the GFP expression levels of the piRNA reporter in the indicated strains grown at 25 °C. **e** Fluorescent micrographs showing the localization of PGL-1::mCardinal, tagRFP::EPS-1, and GFP::NPP-9 in the wild-type germline nucleus. The line in the merged image indicates the position of the line scan for measuring fluorescent intensity across a single germline nucleus. Bars: 2 μm. **f** Fluorescent micrographs showing the co-localization of GFP::EPS-1 and DDX-19::mCherry in the indicated strains. Bars: 10 μm. Right: Pearson's correlation coefficient of GFP::EPS-1 and DDX-19::mCherry signals was analyzed using one-tailed Student's *t*-test. Bars indicate the mean. Errors bars indicate the standard error mean. $n = 25$. **g** Fluorescent micrographs showing the co-localization of tagRFP::EPS-1 and GFP::CSR-1 in the indicated strains. Bars: 10 μm. Right: Pearson's correlation coefficient of tagRFP::EPS-1 and GFP::CSR-1 signals was analyzed using one-tailed Student's *t*-test. Bars indicate the mean. Errors bars indicate the standard error mean. $n = 25$. **h** Fluorescent intensity of granules of indicated markers in the specified strains. Statistical analysis was conducted using a one-tailed Student's *t*-test. Bars indicate the mean. Errors bars indicate the standard error mean. $n = 100$. **i** Mean number of granules of indicated markers per nucleus in the specified strains. Statistical analysis was conducted using a one-tailed Student's *t*-test. Bars indicate the mean. Errors bars indicate the standard error mean. $n = 20$.

investigate how piRNA reporter silencing is enhanced in *npp-14(dz7)*, *npp-24(dz12)*, or *eps-1(dz35)* mutants, we first performed small RNA-seq from mutants grown at 20 °C to examine which step of the piRNA-mediated gene silencing pathways was affected. Unlike *prg-1* mutant, which loses all piRNAs, the overall piRNA levels remained unchanged in *npp-14(dz7)*, *npp-24(dz12)*, and *eps-1(dz35)* mutants (Fig. 6a). Additionally, while the *prg-1* mutant exhibits a drastic reduction of 22G-RNAs at WAGO target genes, the overall levels of these 22G-RNAs remain largely unchanged in the *npp-14(dz7)* mutant, *npp-24(dz12)*, and *eps-1(dz35)* mutants (Fig. 6b). Importantly, when we examine specific piRNA targeting sites, such as the piRNA targeting site of the GFP reporter or the endogenous piRNA target *comt-3*[41], we found that the production of 22G-RNAs was elevated at these sites in *npp-14(dz7)*, *npp-24(dz12)*, and *eps-1(dz35)* mutants (Fig. 6c, d). An similar increase of 22G-RNA levels is observed at these piRNA targeting sites in the *npp-14(dz7)* mutant grown at 25 °C (Fig. S6a, b). These observations suggest that NPP-14, NPP-24, and EPS-1 restrict the local production of 22G-RNA at these piRNA targeting sites.

We next examined the production of 22G-RNAs at piRNA binding sites on a transcriptome-wide scale[42]. Specifically, we compared the levels of 22G-RNAs from WAGO target genes (germline-silenced genes) or from CSR-1 target genes (germline-expressed genes) around predicted piRNA targeting sites[43–45]. Unlike WAGO targets, CSR-1 targets gain resistance to piRNA silencing via CSR-1 small RNAs and consequently only generate low levels of 22G-RNAs at piRNA targeting sites[41,46–48]. In worms grown at 20 °C, 22G-RNA levels were increased at piRNA binding sites of WAGO target genes in *npp-14(dz7)*, *npp-24(dz12)*, and *eps-1(dz35)* mutants (Fig. 6e). In contrast, 22G-RNA levels around the piRNA binding sites of CSR-1 target genes were decreased or unchanged in the *npp-14(dz7)*, *npp-24(dz12)*, and *eps-1(dz35)* mutants (Fig. 6e). In worms grown at 25 °C, the *npp-14(dz7)* mutant exhibited similar increases and decreases in 22G-RNA levels at piRNA targeting sites of WAGO and CSR-1 targets, respectively (Fig. S6c). Together, these results suggest that NPP-14 attenuates the production of WAGO 22G-RNAs at the piRNA binding sites independently of the growth temperature, whether at 20 or 25 °C.

We next investigated whether these elevated 22G-RNAs at WAGO target genes were indeed loaded onto WAGO Argonautes, such as WAGO-1 and HRDE-1. We performed WAGO-1, HRDE-1, and CSR-1 IP and small RNA-seq to measure the levels of small RNA associated with these Argonaute proteins in wildtype and in the *npp-14(dz7)* mutant. We found that WAGO-1 and HRDE-1 bound 22G-RNAs, but not CSR-1 bound 22G-RNAs, were increased at the piRNA reporter mRNA (Fig. S6d). Notably, WAGO-1 22G-RNAs were increased across the piRNA reporter mRNA, whereas HRDE-1 22G-RNAs were increased more locally at the piRNA targeting site in the *npp-14*(dz7) mutant. Transcriptome-wide analyses showed increased levels of WAGO-1 and HRDE-1 associated 22G-RNAs at piRNA binding sites of WAGO targeting genes and decreased levels of CSR-1 associated 22G-RNAs at piRNA targeting sites of CSR-1 targets (Fig. S6e). Taken together, our results suggest that NPP-14, NPP-24, and EPS-1 negatively regulate the production of WAGO 22G-RNAs from the piRNA binding sites.

NPP-14 and EPS-1 maintain the immiscibility of P/Z/M/S germ granule sub-compartments

While PIWI PRG-1 is enriched in P and Z granules, piRNA downstream factors are enriched in various sub-compartments of germ granule, including Z granule, SIMR foci, and Mutator foci[10–12]. To investigate the mechanism by which NPP-14 and EPS-1 attenuate piRNA silencing, we analyzed various markers of these sub-compartments in the mutants. We found that P, Z, granules, S, and Mutator foci markers displayed similar phenotypes in the *npp-14(dz7)* mutant and in the *eps-1(dz35)* mutant: fewer but larger perinuclear foci (Fig. 7a–c and Fig. S7a). The reduction in the number of foci in the *npp-14(dz7)* mutant could not be attributed to decreased protein levels, as western blot analysis of these germ granule proteins indicated largely unchanged levels (Figs. S2e, S7b). Unlike in the wildtype, where germ granules are organized into distinct sub-compartments, the few remaining large germ granules in the *npp-14(dz7)* mutant or in the *eps-1(dz35)* mutant simultaneously contained proteins from P, Z, M, and S sub-compartments (Fig. 7a–c and Fig. S7a). This included increased co-localization between P/Z granule markers with SIMR markers, Mutator markers with SIMR markers, P granule markers with Z granule markers, and Z granule with SIMR markers. Since NPP-14 contains multiple phenylalanine-glycine-glycine (FGG) repeats, which can form a hydrogel with FGG or FG containing factors of NPC and germ granules[19,49], we investigated whether these repeats contribute to NPP-14's role in germ granule organization and piRNA silencing. In the *npp-14(ΔFG)* mutant strain, in which the region containing all FGG repeats was deleted via CRISPR-Cas9 editing, the perinuclear levels of PGL-1::GFP and RFP::ZNFX-1 were reduced. However, we did not observe increased co-localization of P and Z granules or enhanced piRNA reporter silencing (Fig. S7c, d). These findings showed that while FGG repeats may contribute to NPC–germ granule interactions, they are dispensable for NPP-14's roles in germ granule organization or piRNA silencing. We then examined germ granules in the syncytial cytoplasm of the *npp-14(dz7)* mutant and observed that they also simultaneously contained multiple germ granule markers, including P and Z granules, or M and S foci (Fig. S7e, f).

Additionally, we analyzed P body and E granule markers, which are sub-compartments of germ granules but are not known to enrich for piRNA pathway factors. The perinuclear mCherry::CGH-1 foci (a P body marker) appeared more diffuse than other germ granule markers and did not show clear changes in the *npp-14(dz7)* mutant (Fig. S7g). Notably, although the number of E granule EGO-1 foci was reduced in the *npp-14(dz7)* mutant, they did not exhibit increased co-localization with the P granule marker PGL-1 (Fig. S7h, i). Therefore, not all germ granule sub-compartments display enhanced co-localization in the

https://doi.org/10.1038/s41467-025-59526-3

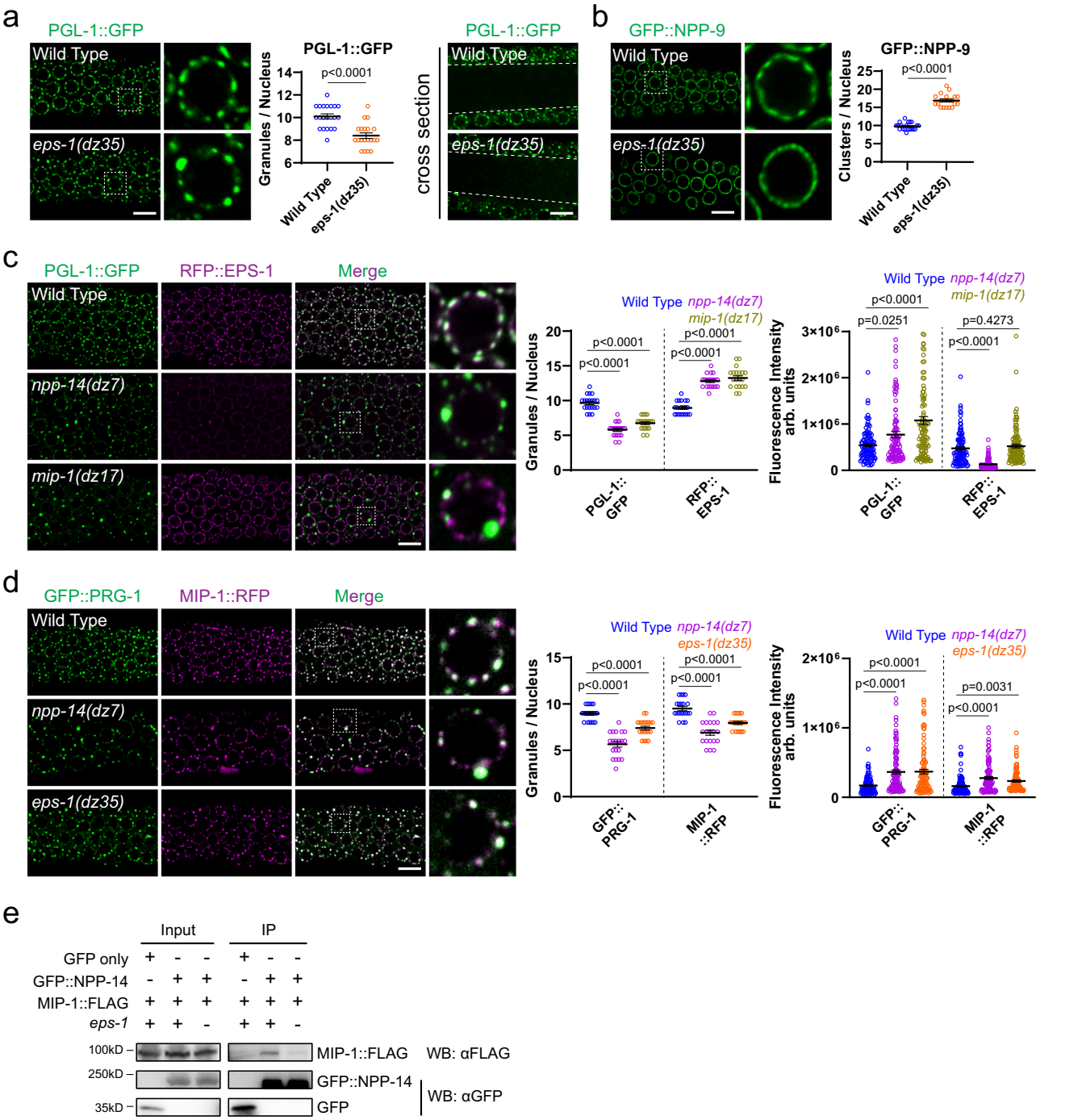

Fig. 5 | EPS-1 promotes germ granule–NPC interaction. a Fluorescent micrographs showing the localization of PGL-1::GFP in the germline nucleus and syncytial cytoplasm in the indicated strains. Bars: 10 μm. Mean number of granules per nucleus was analyzed using a one-tailed Student's *t*-test. Bars indicate the mean. Errors bars indicate the standard error mean. $n = 20$. **b** Fluorescent micrographs showing the localization of GFP::NPP-9 in the indicated strains. Bars: 10 μm. Mean number of clusters per nucleus was analyzed using a one-tailed Student's *t*-test. Bars indicate the mean. Errors bars indicate the standard error mean. $n = 20$. **c**, **d** Fluorescent micrographs showing the location and expression levels of **c** PGL-1::GFP and tagRFP::EPS-1 and **d** GFP::PRG-1 and MIP-1::tagRFP in the indicated strains. Bars: 10 μm. Right: mean number of granules per nucleus ($n = 20$) or fluorescent intensity of granules ($n = 100$) was analyzed using one-way ANOVA followed by Dunnett's correction for multiple comparisons. Bars indicate the mean. Errors bars indicate the standard error mean. **e** Cross-linking and coIP analyses showing the interaction between NPP-14 and MIP-1 in the indicated strains. Antibodies against GFP and FLAG were employed. Source data are provided as a Source Data file.

npp-14(dz7) mutant. Taken together, our analyses highlight the roles of NPP-14 and EPS-1 in maintaining proper germ granule architecture and ensuring the organization of distinct P, Z, S, and M sub-compartments.

Similar to the *eps-1* mutant, fewer PRG-1 foci are observed in both the *mip-1* or *ddx-19* RNAi-treated animals (Fig. 4c). We sought to investigate why *mip-1* or *ddx-19* RNAi did not enhance piRNA reporter silencing. Notably, we did not observe increased co-localization between P and Z granule markers (Fig. S7k–m) and only a mild increase of co-localization between S and M foci in the *mip-1(dz17)* mutant (Fig. S7m–o), consistent with a recent report indicating that

https://doi.org/10.1038/s41467-025-59526-3

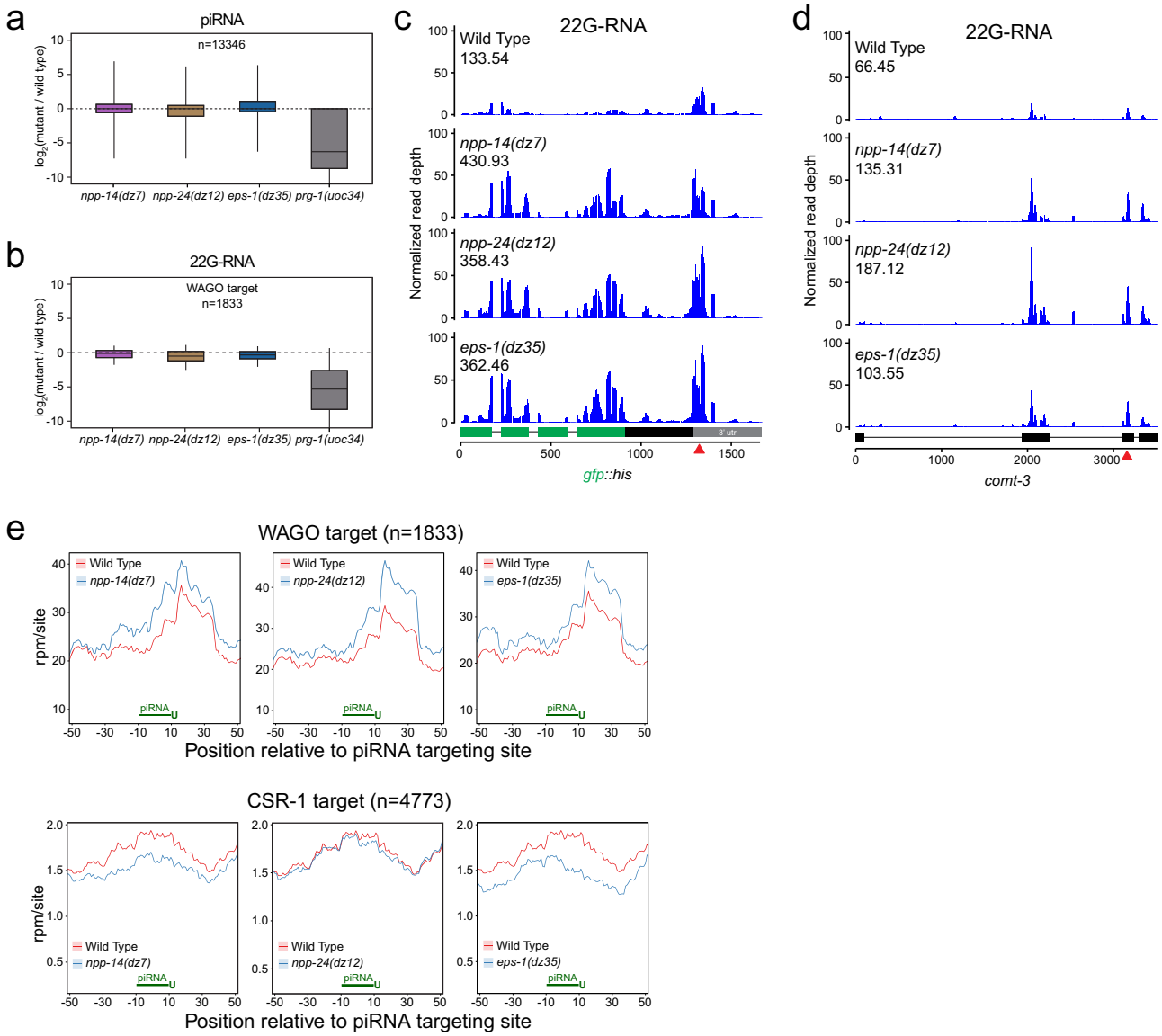

Fig. 6 | NPP-14, NPP-24, and EPS-1 restrict the amplification of secondary small RNAs at piRNA targeting sites. a Boxplots showing the fold change of piRNA expression levels in the indicated strains compared to the wildtype. Lines represent median values, boxes represent first and third quartiles, and whiskers display 5th and 95th percentiles. **b** Boxplots showing the fold change of 22G-RNA expression levels against WAGO targets in the indicated strains compared to the wildtype. Lines represent median values, boxes represent first and third quartiles, and whiskers display 5th and 95th percentiles. **c** Distribution and levels of antisense 22G-RNAs mapped to the piRNA reporter sequences in the indicated strains. Total counts of mapped antisense 22G-RNA reads are indicated. The red arrowhead indicates the location of sequences complementary to the endogenous piRNA *21ur-1*. **d** Distribution and levels of antisense 22G-RNAs mapped to the endogenous piRNA targeting gene *comt-3* sequences in the indicated strains. Total counts of mapped antisense 22G-RNA reads are indicated. The red arrowhead indicates the location of the predicted piRNA targeting site. **e** Density of 22G-RNAs within a 100-nt window around predicted piRNA targeting sites in the indicated strains. Computed by summing 22G-RNA density per piRNA targeting site in WAGO targets (top) or CSR-1 targets (bottom). The plots are centered on the 10th nucleotide of piRNAs.

these foci do not exhibit enhanced co-localization in the *mip-1* mutant[14]. In addition, we did not detect a significant increase in co-localization between P and M foci in the *ddx-19(dz21)* mutant (Fig. S7m, p, q). The lack of strong co-localization changes in the *mip-1(dz17)* and *ddx-19(dz21)* mutants indicates that the enhanced piRNA silencing observed in *npp-14* or *eps-1* mutants may result from germ granule disorganization.

Enlarged and disorganized germ granules in the *npp-14* mutant are enriched with prominent pUG RNA foci

As described earlier, P granules, a sub-compartment of germ granules, are known to be the major sites of mRNA export in the germline of *C. elegans*[20]. Since fewer and larger germ granules are found in the *npp-14(dz7)* mutant, we investigated whether mRNA export and localization is affected and if mRNA exhibits co-localization with germ granule. We performed smFISH against PolyA RNAs in the *npp-14(dz7)* mutant. In wild-type animals, in addition to the cytoplasmic signal, PolyA RNAs were accumulated at perinuclear foci (Fig. S8a). In the *npp-14(dz7)* mutant, while PolyA RNAs were also present in the cytoplasm, the number of perinuclear foci was significantly reduced. Additionally, poly(A) RNA FISH combined with PRG-1 immunostaining revealed a modest but significant increase in the co-localization of poly(A) RNA foci with PRG-1 foci in *npp-14(dz7)*, *npp-24(dz12)*, and *eps-1(dz35)* mutants (Fig. 8a and Fig. S8b). This suggests that mRNAs may accumulate or undergo altered export at those perinuclear germ granules observed in these mutants.

https://doi.org/10.1038/s41467-025-59526-3

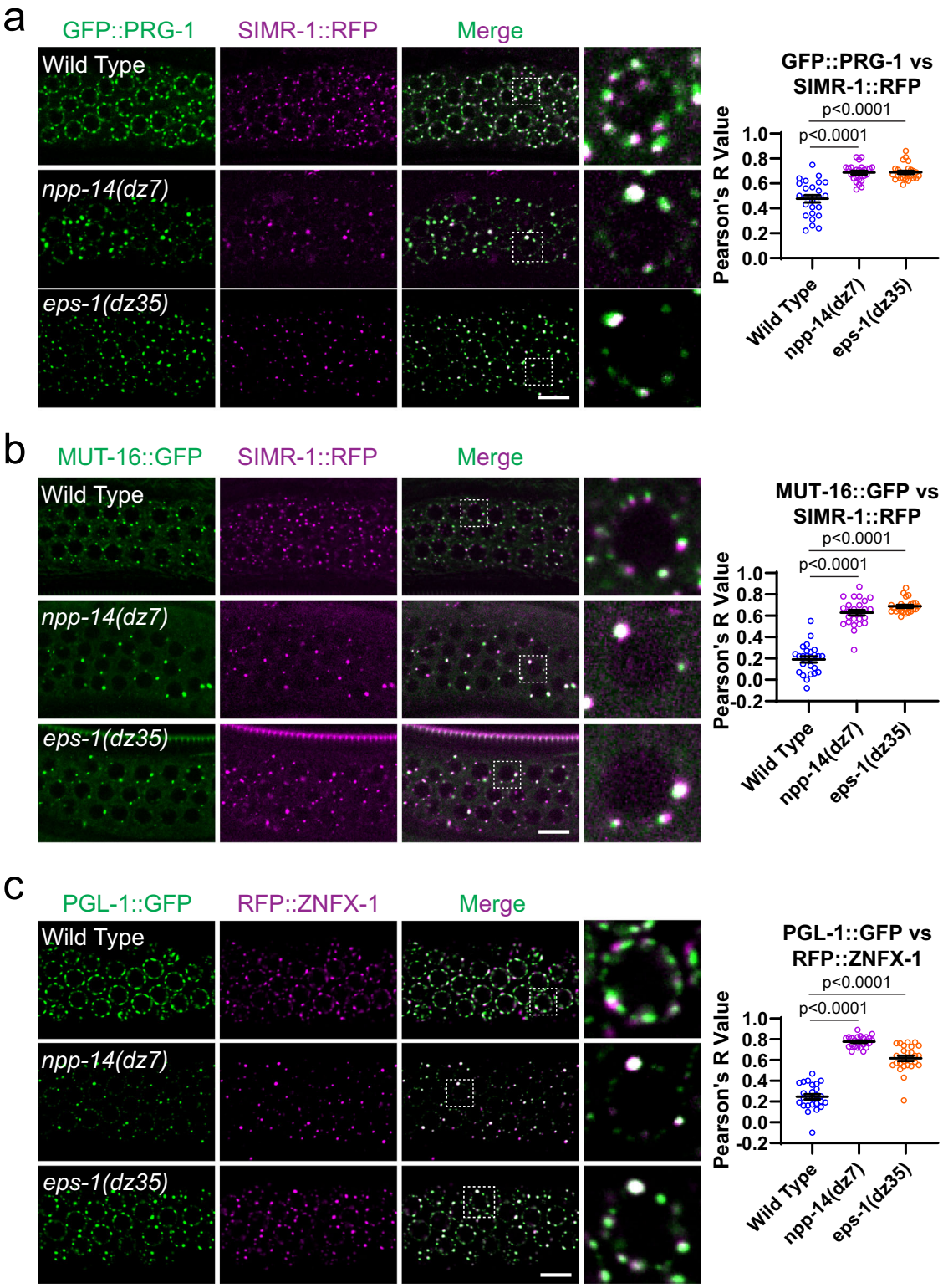

Fig. 7 | NPP-14 and EPS-1 maintain the immiscibility of germ granule sub-compartments. a–c Fluorescent micrographs showing the co-localization of **a** GFP::PRG-1 and SIMR-1::tagRFP, **b** MUT-16::GFP and SIMR-1::tagRFP, and **c** PGL-1::GFP and tagRFP::ZNFX-1 in the indicated strains. Bars: 10 μm. Right: Pearson's correlation coefficient of indicated marker signals was analyzed using one-way ANOVA, followed by Dunnett's correction for multiple comparisons. Bars indicate the mean. Errors bars indicate the standard error mean. $n = 25$.

Once piRNA recognizes its mRNA targets, additional piRNA pathway factors RDE-8 and RDE-3/MUT-2 are recruited to cleave and to add polyUG RNA tails (pUG RNAs) on the mRNA targets, respectively[50,51]. pUG RNAs act as a key signal that recruits RNA-dependent RNA polymerase to produce downstream WAGO 22G-RNAs[51]. As WAGO 22G-RNAs are increased from piRNA targeting sites in the *npp-14(dz7)* mutant, we asked whether pUG RNAs are accumulated in perinuclear germ granules in the *npp-14(dz7)* mutant. By using

https://doi.org/10.1038/s41467-025-59526-3

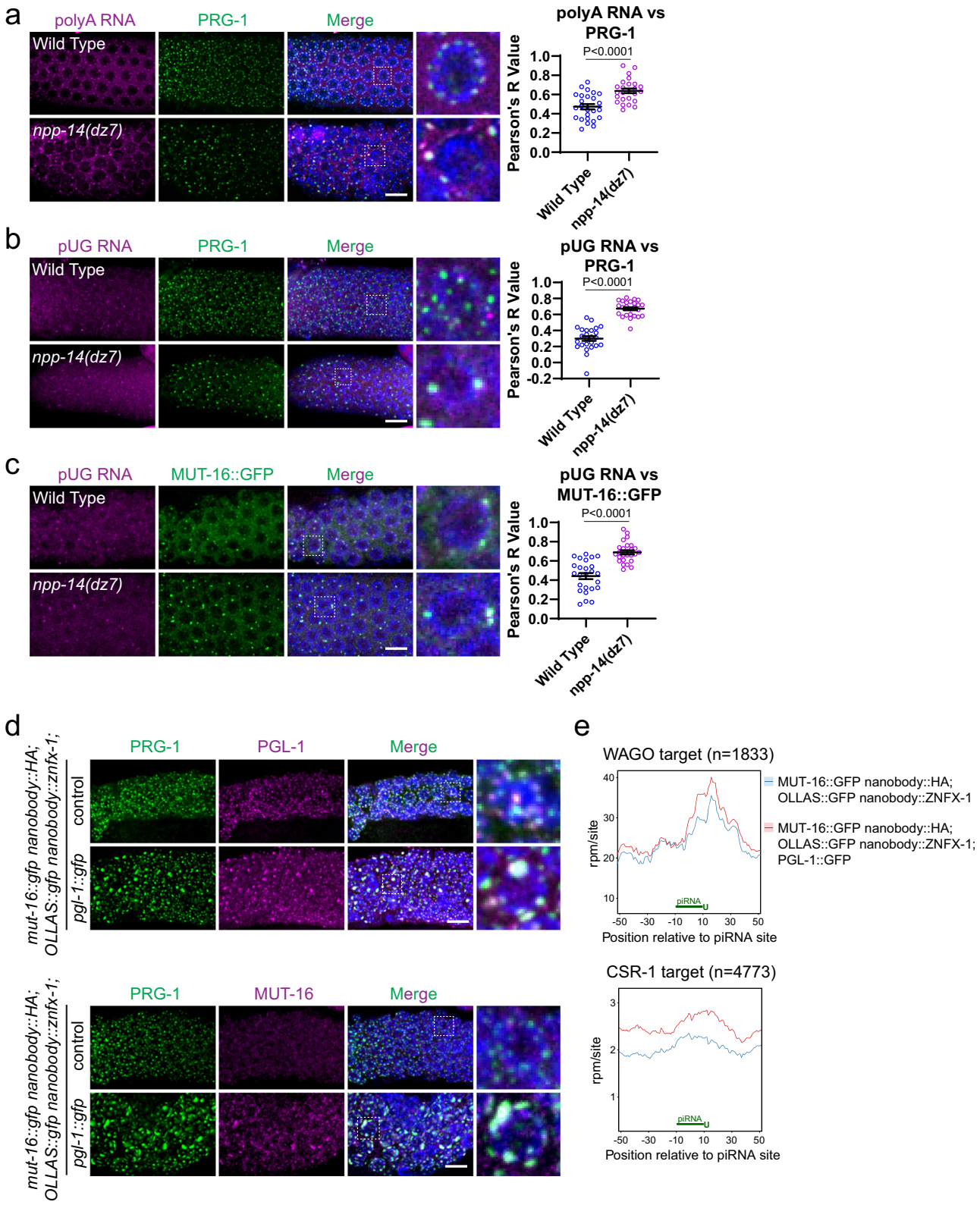

smFISH and immunostaining, we found that more prominent pUG RNA foci were found in the *npp-14(dz7)* mutant, in the *npp-24(dz12)* mutant, or in the *eps-1(dz35)* mutants than those observed in wild-type animals, and many of these large pUG RNA foci were co-localized with PIWI PRG-1 or Mutator foci markers MUT-16 (Fig. 8b, c and Fig. S8c). These results show those enlarged germ granules found in *npp-14*, *npp-14*, or *eps-1* mutant animals are enriched with pUG RNAs.

Tethering of PZM sub-compartments enhances 22G-RNA production at piRNA targeting sites

As described above, piRNA pathway factors involved in initiation and amplification are enriched in distinct germ granule sub-compartments[14]. Our observation that P/Z/M/S foci exhibit increased co-localization in *npp-14(dz7)* and *eps-1(dz35)* mutants suggests that this enhanced co-localization may contribute to the observed increase

Fig. 8 | Enlarged and disorganized germ granules serve as sites for gene silencing. a Fluorescent micrograph of pachytene nuclei in fixed adult gonads hybridized with a fluorescent polyT probe complementary to polyA RNA and immunofluorescence stained with antibodies against PRG-1 in the indicated strains. Nuclear DNA was stained with DAPI (Blue). Bars: 10 μm. Right: Pearson's correlation coefficient of polyA RNA foci with PRG-1 foci was analyzed using one-tailed Student's *t*-test. Bars indicate the mean. Errors bars indicate the standard error mean. $n = 25$. **b**, **c** Fluorescent micrographs of pachytene nuclei of fixed adult gonads hybridized with a fluorescent probe complementary to pUG RNA and immunofluorescence stained with antibodies against **b** PRG-1 or **c** GFP in the indicated strains. Bars: 10 μm. Right: Pearson's correlation coefficient of pUG RNA foci with PRG-1 foci or with MUT-16::GFP foci was analyzed using one-tailed Student's *t*-test. Bars indicate the mean. Errors bars indicate the standard error mean. $n = 25$. **d** Fluorescent micrographs of pachytene nuclei of fixed adult gonads immunofluorescence stained with antibodies against PRG-1 and GFP (top), and PRG-1 and HA (bottom) in the indicated strains. Bars: 10 μm. **e** Density of 22G-RNAs within a 100-nt window around predicted piRNA targeting sites in the indicated strains. Computed by summing 22G-RNA density per piRNA targeting site in WAGO targets (top) or CSR-1 targets (bottom). The plots are centered on the 10th nucleotide of piRNAs.

in piRNA silencing in these mutants. If so, artificially bringing these sub-compartments together should similarly enhance 22G-RNA production at piRNA target sites. A transgenic strain expressing GFPnanobody-tagged MUT-16 and ZNFX-1 was generated in previous studies[52]. By crossing this strain with one carrying PGL-1-GFP, the GFPnanobody-tagged MUT-16 and ZNFX-1 should be tethered to PGL-1-GFP. Indeed, immunostaining for PGL-1 (P granule marker), PRG-1 (P/Z granule marker), and MUT-16 (Mutator marker) confirmed that co-localization of these foci was significantly enhanced in the PZM-tethered strain compared to controls (Fig. 8d). This tethered strain also recapitulated the 22G-RNA level changes observed in *npp-14(dz7)* mutants, showing increased 22G-RNA production at WAGO targets (Fig. 8e). These results demonstrate that artificial tethering of PZM granules is sufficient to enhance 22G-RNA production at piRNA target sites of WAGO targets. Collectively, our imaging analyses, germ granule tethering assay, and small RNA sequencing data are consistent with a model in which enlarged granules, composed of fused P, Z, M, S sub-compartments, contribute to the increased production of secondary WAGO 22-RNAs at piRNA targeting sites in the *npp-14, npp-24 and eps-1* mutants.

Impairment of RNAi silencing and inheritance in the *npp-14* mutant

piRNAs and siRNAs share common downstream WAGO 22G-RNA pathway factors to trigger gene silencing, and previous studies have suggested that these two pathways can compete for downstream gene silencing machinery[6]. In the *prg-1* mutant animals, which lose all piRNAs, RNAi inheritance is greatly enhanced[6]. Given the enhanced piRNA-mediated gene silencing found in the *npp-14(dz7)* mutant, we wondered whether the efficiency of RNAi may be affected. To compare the germline RNAi efficiency, we assessed the ratio of dead embryos upon *pos-1* RNAi. *Pos-1* is a maternally expressed gene required for embryonic viability[53]. While the treatment of undiluted *pos-1* dsRNA-expressing bacteria led to nearly 100% lethality in both wild-type and the *npp-14(dz7)* null mutant animals, treatment with diluted *pos-1* dsRNA-expressing bacteria led to a smaller portion of dead embryos in the *npp-14(dz7)* null mutant than in wild-type animals (Fig. S9a). This result suggests that the RNAi efficiency is compromised in the *npp-14(dz7)* mutant.

If the RNAi defects observed in *npp-14, npp-24, and eps-1* mutants are caused by enhanced piRNA silencing, we would expect that the loss of piRNAs would rescue these RNAi defects. However, we found that in the *prg-1* mutant, which lacks all piRNAs, the RNAi defects of these mutants were only partially rescued (Fig. S9a, b). This observation suggests that either the RNAi defects are independent of piRNA silencing or that other endogenous small RNA pathways also contribute to the RNAi defects observed in these mutants.

Proper germ granule organization has been linked to RNAi inheritance[10,54,55]. We next asked whether RNAi inheritance is compromised in the *npp-14* mutant. In these experiments, we treated a GFP::histone-expressing strain with GFP dsRNA-expressing bacteria for one generation[55]. The animals were then treated with bleach to obtain their embryos and to avoid bacterial contamination across generations. The embryos of each following generation were cultured on control food to determine the ratio of GFP-silenced animals (Fig. 9a). We found that GFP RNAi treatment could completely silence GFP::histone signals in both the wildtype and the *npp-14(dz7)* mutant animals. Notably, in the each of the following three generations on control food, while 100, 73, and 55% of wild-type animals still exhibited no GFP signals, only 80, 20, and 16% of the *npp-14(dz7)* mutant animals exhibited no GFP signals (Fig. 9b, c). Additionally, we sequenced small RNAs and compared the abundance of 22G-RNAs targeting GFP mRNAs. We found that those 22G-RNAs targeting GFP mRNAs were slightly decreased in the *npp-14(dz7)* mutant compared to wild type in the P0 generation but were significantly more decreased in the first generation after removal of the RNAi bacteria (Fig. 9d). Collectively, our data show that the efficiency of both RNAi and RNAi inheritance are compromised in the *npp-14* mutant animals. These findings underscore the importance of NPP-14 in regulating the efficacy of both the siRNA and piRNA pathways in germ cells (Fig. 9e).

Discussion

Perinuclear germ granules are conserved features observed across diverse organisms[15–18], yet the factors mediating their association with nuclear pore complexes (NPCs) remain largely unknown. In this study, we investigated the regulation of gene silencing and germ granule–NPC interactions in *C. elegans*, identifying the pivotal roles of two nucleoporins, NPP-14 and NPP-24, as well as the germ granule factor EPS-1, in mediating germ granule–NPC interactions. We characterized EPS-1 as a D granule factor[14] positioned between the P granule sub-compartment and NPCs. Importantly, we found that the association between MIP-1 and NPP-14 was compromised in the *eps-1* mutant, highlighting the role of EPS-1 in promoting germ granule–NPC interactions. Collectively, our findings uncover key NPC and germ granule factors that mediate germ granule–NPC interactions.

In *C. elegans*, germ granules assemble at NPC clusters in the germline[16,19]. Our results also reveal a strong interdependence between NPC clustering and germ granule–NPC association. First, we observed that NPC components NPP-14 and NPP-24 promote both germ granule tethering and nuclear pore clustering. In the *npp-14* mutants, germ granules marker PGL-1 foci became rounder, detached from the nuclear periphery, and exhibited increased fusion events. The weakened anchoring of germ granules correlates with reduced NPC clustering. Additionally, germ granule factors also influence NPC clustering −mutants lacking EPS-1, MIP-1, or MIP-1 and MIP-2 exhibited rounder and larger germ granules alongside defects in NPC clustering. Together, our findings suggest that robust germ granule–NPC interactions promote NPC clustering, while NPC clusters, in turn, provide a platform for stable germ granule tethering. This relationship underscores the broader biological relevance of NPC clustering, which has been observed in germ cells of many animals[20–22].

How germ granules are organized into distinct sub-compartments were unclear. Notably, in *npp-14* or *eps-1* mutants, we observed increased co-localization of P/Z/M/S foci−sub-compartments enriched with initiation and amplification factors of the piRNA silencing pathway. Given that NPP-14 and EPS-1 play critical roles in NPC–germ granule interactions, our findings suggest that these interactions contribute to proper germ granule organization, potentially by

https://doi.org/10.1038/s41467-025-59526-3

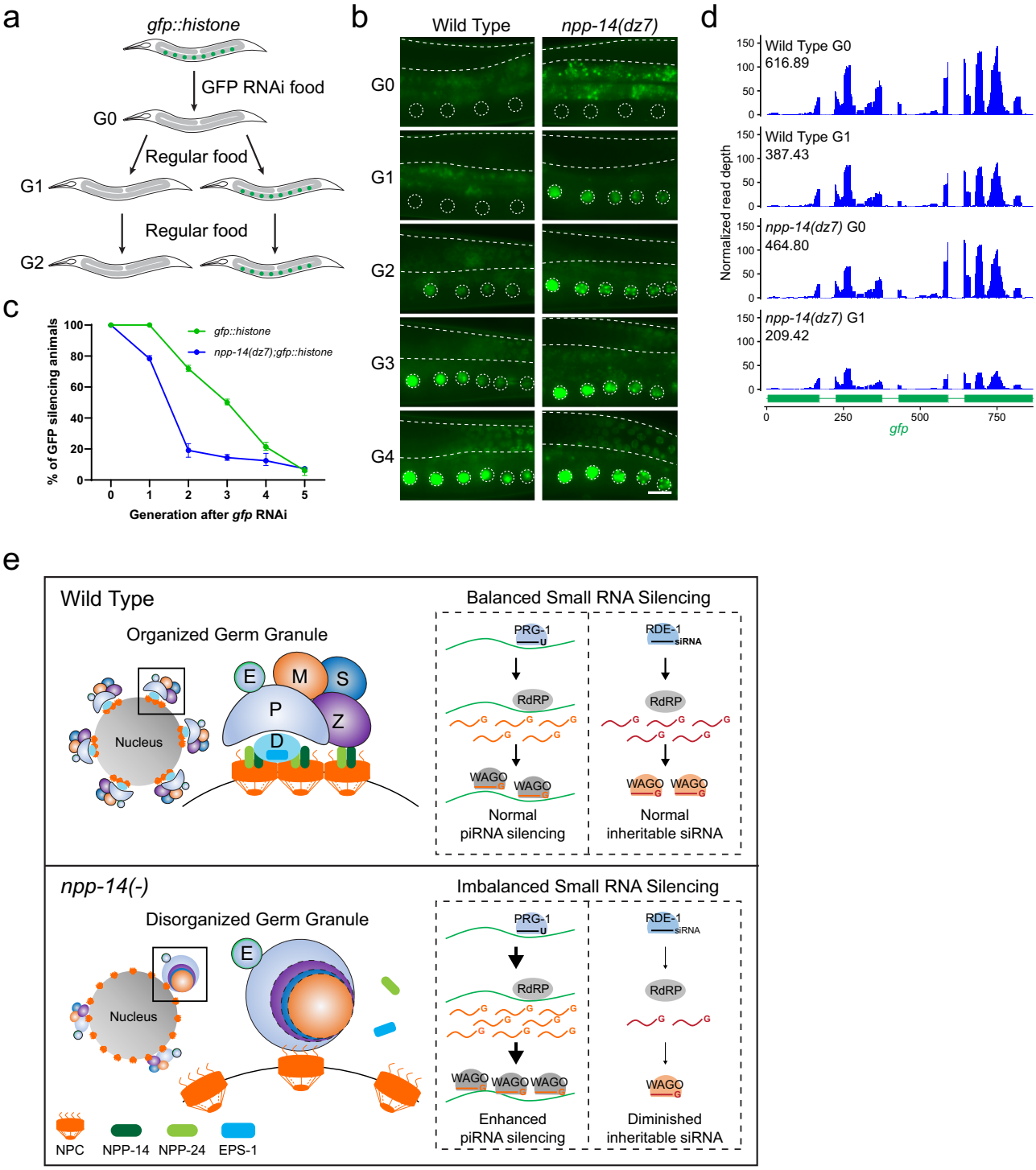

Fig. 9 | RNAi inheritance is compromised in the *npp-14* mutant. a A schematic illustrating the RNAi assay with a GFP::histone reporter to assess the mutant's ability to initiate RNAi and to inherit gene silencing over generations. **b** Representative fluorescent micrographs showing the GFP::histone reporter in the RNAi-treated generation (G0) or the subsequent generations (G1 to G4) in the indicated strains. Dashed lines and circles denote the germline and maturing oocyte nuclei, respectively. Note that the bright signals observed outside of dashed areas are autofluorescence signals originating from gut granules. Bars: 10 μm. **c** Percentage of screened animals showing GFP reporter silencing in the indicated strains. Data points represent the mean, with error bars indicating the standard error of the mean. Distributions represent data collected from three independent experiments. **d** Distribution and levels of the antisense 22G-RNAs mapped to GFP coding sequences in the indicated strains from the RNAi-treated generation G0 and the subsequent generation G1. Total counts of mapped antisense 22G-RNA reads are indicated. **e** A model depicting the role of NPP-14, NPP-24, and EPS-1 in germ granule organization and its role in balancing small RNA gene silencing pathways.

establishing polarization of germ granule factors. In this model, when P granule factors fail to interact with NPCs, they instead interact with factors from other sub-compartments, leading to their enhanced co-localization and subsequent loss of organization. Similarly, our recent study identified germline P bodies are situated between P and Z granules, and mutation of P body factors CGH-1 or CAR-1 compromised P and Z granule organization[28]. Moreover, a recent study shows that the loss of the P granule assembly factor MIP-1, which is spatially

situated between D and E granules, leads to enhanced co-localization of D and E granules but not P/Z/M/S foci[14]. Therefore, these findings support a model in which interactions between specific key factors contribute to the organization of biological condensates, refining the current model that attributes condensate organization mainly to the individual biophysical properties of constituent factors[56].

The enhanced piRNA silencing observed in the *npp-14*, *npp-24*, or *eps-1* mutants was linked to the presence of enlarged and disorganized perinuclear germ granules in these mutants. Our findings support a model in which increased co-localization of PIWI PRG-1 and downstream silencing factors triggers enhanced piRNA silencing. In support of this model, these unorganized germ granules were enriched with enlarged polyUG RNA foci, signals for small RNA amplification[51]. Furthermore, tethering of Mutator (MUT-16) and Z granule (ZNFX-1) factors[52] to P granules (PGL-1) was sufficient to drive an increased production of secondary WAGO 22G-RNAs at piRNA-targeting sites, supporting that increased co-localization of PZMS granules leads to excessive amplification of piRNA silencing signals in the *npp-14*, *npp-24*, or *eps-1* mutants. Therefore, our findings highlight the importance of germ granule architecture in gene silencing and have broad implications for cellular condensate organization in gene regulation.

Interestingly, while piRNA silencing was enhanced in the *npp-14* mutant, RNAi silencing and its inheritance were compromised, highlighting a critical role for germ granule–NPC interactions in both siRNA- and piRNA-mediated gene silencing—two major small RNA-based genome defense pathways in animals. Loss of piRNAs only partially rescued the RNAi defects of the *npp-14* mutant, implying that either RNAi defects and the enhanced piRNAs are independent in this context, or additional small RNA pathways also contribute to the RNAi defects observed in the *npp-14* mutant. Notably, while multiple Argonaute proteins, including PRG-1 (piRNA Argonaute), ALG-3/4, and CSR-1 are enriched in germ granules[57], whereas RDE-1 (siRNA Argonaute) is not. Given that different foreign/selfish RNAs may be encountered in distinct cellular locations—such as transposon-derived RNAs within the nucleus or viral dsRNAs in the cytoplasm—our study raises an interesting model in which the compartmentalization of small RNA silencing factors has evolved to optimize genome defense mechanisms against diverse classes of foreign nucleic acids.

Methods

Caenorhabditis elegans strains

Animals were at either 20 or 25 °C cultured on standard nematode growth media (NGM) plates seeded with the *E. coli* OP50 strain. The Bristol strain N2 was utilized as the standard wild-type strain. Details of the strains employed in this study can be found in Supplementary Data 2.

Brood size

L4 stage hermaphrodites (P0) were individually placed onto freshly seeded NGM plates and allowed to grow for 24 h at either 20 or 25 °C. P0 adults were transferred to new NGM plates every 24 h until they no longer laid eggs. All the F1 progeny were counted. The brood size of each P0 animal is the total sum of F1 progeny across all plates where the P0 animal laid eggs. At least eight individual P0 animals were used to score the brood size for each strain.

RNAi and RNAi inheritance assay

E. coli HT115 (DE3) strains expressing dsRNAs against target genes were obtained from *C. elegans* RNAi collection derived from the *C. elegans* ORFeome Library v1.1 (Horizon Discovery) or homemade strains. To prepare the RNAi bacterial cultures, Luria broth supplemented with 100 μg/mL ampicillin was inoculated with the respective bacterial strain and incubated overnight at 37 °C. The cultures were then seeded onto NGM plates containing 100 μg/mL ampicillin and 1 mM IPTG and incubated at room temperature for 1 to 2 days to induce dsRNA expression. RNAi experiments were conducted at either 20 or 25 °C by transferring synchronized L1s or L4s onto NGM plates seeded with RNAi bacteria. Adults (transferred at the L1 stage) or progeny adults (transferred at the L4 stage) were subjected to imaging and phenotype scoring. For the *pos-1* RNAi treatment, *pos-1* RNAi bacteria were diluted with control RNAi bacteria expressing empty vector L4440.

For the RNAi inheritance assay, synchronized L1 animals of the indicated genotypes were exposed to bacteria expressing GFP dsRNA. F1 embryos were collected by hypochlorite/NaOH bleach treatment and subsequently cultured on NGM plates seeded with *E. coli* OP50. GFP expression in both the parental generation and progeny were imaged and scored. The silenced GFP reporter was characterized by the absence of GFP or dim GFP expression, while the desilenced GFP reporter was characterized by robust GFP expression. Images were captured using a Zeiss Axio Imager M2 compound microscope with a Plan-Apochromat 40x/1.4 Oil objective.

CRISPR/Cas9-mediated gene editing and transgenes

CRISPR/Cas9-mediated gene editing experiments were conducted using Cas9/sgRNA ribonucleoprotein (RNP) strategies. The sgRNAs for CRISPR/Cas9 gene editing were transcribed in vitro using the HiScribe T7 Quick High Yield RNA Synthesis Kit (New England Biolabs, E2050S) and purified with the Monarch RNA Cleanup Kit (New England Biolabs, T2040L). The 3xFLAG/GFP/tagRFP tag sequence (short donor) and a tag sequence containing short 5′ and 3′ homology sequences (~40 nt) (long donor) were amplified by PCR. The purified 1.2 μg of short donor and 1.2 μg of long donor products were subjected to a denaturation and renaturation process (95 °C for 2 min, 85 °C for 10 s, 75 °C for 10 s, 65 °C for 10 s, 55 °C for 1 min, 45 °C for 30 s, 35 °C for 10 s, 25 °C for 10 s, and held at 4 °C) to generate hybrid DNA donor templates. The final concentrations of the injection mixture were as follows: 250 ng/μL of Alt-R S.p. Cas9 Nuclease V3 (Integrated DNA Technologies), 200 ng/μL of in vitro synthesized sgRNA, 200 ng/μL of hybrid DNA donor, and 40 ng/μL of co-injection marker pRF4. Cas9 and sgRNA were mixed and incubated at 37 °C for 10 min before adding other components. The injection mixtures were microinjected into the gonads of adult *C. elegans*. The F1 roller progeny were individually collected and genotyped by PCR to identify the desired transgenes. Sequences of alleles created in this study can be found in the Supplementary Information. Sequences of primers and oligos used in this study can be found in Supplementary Data 3.

Mos1-mediated single copy insertion (MosSCI) was used to generate the *pie-1p::turboID::3xha* transgenic strain. Final concentrations of injection mixture were as follows: 50 ng/μL of pCFJ601 (eft-3p::transposase), 2.5 ng/μL of pCFJ90 (myo-2p::mCherry), 5 ng/μL of pCFJ104 (myo-3p::mCherry), and 50 ng/μL of pDZ615 (pie-1p::turboID::3xha::pie-1 3′utr in pCFJ150). EG8081 (unc-119(ed3) III; oxTi177 IV) was used for injection. Two injected animals were placed on each seeded NGM plate and cultured at 25 °C. Plates were screened for animals exhibiting normal movement but lacking the red co-injection markers.

Fluorescence microscopy and image processing

Fluorescent proteins were observed in living nematodes by mounting young adult animals on 2% agarose pads with M9 buffer (22 mM KH_2PO_4, 42 mM Na_2HPO_4, 86 mM NaCl) supplemented with 50 mM levamisole. Images were captured using either a Zeiss LSM800 confocal microscope with a Plan-Apochromat 63x/1.4 Oil DIC M27 objective or a Zeiss Axio Imager M2 compound microscope with a Plan-Apochromat 40x/1.4 Oil objective.

Images were processed and quantified using ImageJ. To assess the fluorescence intensity of individual granules, regions of the gonad pachytene were selected, and fluorescence thresholds were automatically set using the Yen threshold method to identify fluorescent puncta within the pachytene region. Fluorescent puncta larger than 10 pixels^2 were analyzed.

To assess granule densities surrounding the nucleus, 20 nuclei in each germline pachytene region were randomly selected, and perinuclear puncta were manually counted. To assess granule densities within the pachytene region, images of the gonad pachytene were selected and defined as regions of interest (ROIs). Fluorescence thresholds were automatically set using the Yen threshold method to identify fluorescent puncta within the ROIs. Fluorescent puncta larger than 10 pixels^2 were analyzed, and the areas of the ROIs were measured. Granule density was calculated by dividing the number of fluorescent puncta within an ROI by the ROI area.

To assess co-localization between two granules, the fluorescence of individual granules was automatically thresholded, and a white mask was generated. Co-localization of the two granules was analyzed using the Coloc2 plug-in.

Quantification data were analyzed using Student's *t*-test or one-way ANOVA, followed by Dunnett's correction for multiple comparisons.

Western blotting

Lysates were prepared from 100 synchronized young adult worms. The worms were boiled in boiling buffer (100 mM Tris-HCl (pH 6.8), 8% SDS, 20 mM β-mercaptoethanol) for 10 min and then in 1x SDS loading buffer for an additional 5 min. Proteins were separated by standard SDS-PAGE and transferred to PVDF membranes (Roche) using the Trans-Blot Turbo Transfer System (Bio-Rad). The membranes were blocked in 5% skimmed milk in TBST (20 mM Tris-HCl pH 7.4, 150 mM NaCl, and 0.05% Tween-20) for 1.5 h at room temperature and then incubated with primary antibodies overnight at 4 °C. After five washes with TBST buffer, membranes were incubated with secondary antibodies for 1.5 h at room temperature then washed five times with TBST. ECL substrates were used for the detection of protein bands and images were obtained by a Tanon 5200 Chemiluminescent Imaging System (Tanon). The antibodies used in this study were anti-GFP (Santa Cruz, sc-9996) at 1:500 dilution, anti-HA (Cell Signaling Technology, 3724S) at 1:1000 dilution, anti-FLAG (Sigma-Aldrich, F1804) at 1:1000 dilution, anti-α-Tubulin (Sigma-Aldrich, T6199) at 1:1500 dilution, HRP-conjugated Goat Anti-Mouse IgG (H + L) (Proteintech, SA00001-1) at 1:5000 dilution, and HRP-conjugated Goat Anti-Rabbit IgG (H + L) (ZSGB-Bio, ZB-2301) at 1:5000 dilution.

TurboID-based proximity labeling

Approximately 150,000 synchronized young adults were washed three times with M9 buffer and subsequently incubated in M9 buffer supplemented with 1 mM biotin for 2 h at 20 °C. After incubation, the worms underwent three washes in M9 buffer followed by one wash in pre-cooled ddH_2O. Animals were flash-frozen in liquid nitrogen and stored at −80 °C until further use.

Two volumes of RIPA buffer (50 mM Tris-HCl pH 7.5, 150 mM NaCl, 0.5% sodium deoxycholate, 1% NP-40) supplemented with 1x protease inhibitor cocktail without EDTA (Promega, G6521) were added to one volume of packed worms, which were then ground in a glass grinder eight to ten times on ice within a 10-min timeframe. Lysates were clarified by centrifugation at 20,000 × *g*, 4 °C, for 15 min. The resulting supernatants were desalted using Zeba spin desalting columns 7K MWCO (Thermo Scientific, 89890) to remove excess free biotin from the labeling process, followed by incubation with Dynabeads MyOne streptavidin C1 (Invitrogen, 65002) in RIPA buffer at room temperature for 30 min on a rocker. Beads were washed five times with RIPA buffer and twice with 1x PBS buffer. After removing excess buffer, the beads were stored at −80 °C for mass spectrometry analysis.

Mass spectrometry analysis

Streptavidin beads were boiled in SDT buffer (4% SDS, 100 mM Tris-HCl, pH 7.6) supplemented with 100 mM dithiothreitol for 5 min. After cooling, the beads were then washed three times with 50 mM ammonium bicarbonate, then incubated with 50 mM iodoacetamide in the dark at room temperature for 30 min. After incubation, beads were mixed with 6 μg of trypsin (Promega, V5113) in 40 μL of 50 mM ammonium bicarbonate and digested at 37 °C for 16–18 h. The supernatant containing the released peptides was collected. The peptides were desalted using C18 StageTip for subsequent LC-MS/MS analysis. LC-MS/MS analysis was conducted using a Q Exactive Plus mass spectrometer coupled with an Easy 1200 nLC system (Thermo Fisher Scientific). Initially, peptides were loaded onto a trap column (100 μm × 20 mm, 5 μm, C18, Dr. Maisch GmbH) with buffer A (0.1% formic acid in water). For reverse-phase high-performance liquid chromatography (RP-HPLC) separation, an EASY-nLC system (Thermo Fisher Scientific, Bremen, Germany) equipped with a self-packed analytical column (75 μm × 150 mm; 3 μm ReproSil-Pur C18 beads, 120 Å, Dr. Maisch GmbH) was used at a flow rate of 300 nL/min. Mobile phase A consisted of 0.1% formic acid in water, while mobile phase B was 0.1% formic acid in 95% acetonitrile. Peptides were eluted over 120 min using a linear gradient of buffer B. Mass spectrometry data were acquired employing a data-dependent top 20 method that dynamically selected the most abundant precursor ions from the survey scan (300–1800 m/z) for higher-energy collisional dissociation (HCD) fragmentation. Peptide recognition mode was enabled during the analysis, with a lock mass of 445.120025 Da utilized for internal mass calibration. Full MS scans were acquired at a resolution of 70,000 at m/z 200, and MS/MS scans at a resolution of 17,500 at m/z 200. The maximum injection time was set to 50 ms for both MS and MS/MS scans. The normalized collision energy was 27, and the isolation window for precursor ion selection was set to 1.6 Th. Dynamic exclusion was applied with a duration of 60 s. The MS data of three biological replicates were analyzed using MaxQuant software version 1.6.0.16. MS data were searched against the Uniprot Protein Database: species *C. elegans* uniprot-*C. elegans* [6239]-27419-20210222.fasta. The trypsin was selected as a digestion enzyme. The maximal two missed cleavage sites and the mass tolerance of 4.5 ppm for precursor ions and 20 ppm for fragment ions were defined for database search. Carbamidomethylation of cysteines was defined as a fixed modification, while acetylation of protein N-terminal, oxidation of methionine was set as variable modifications for database searching. Label-free quantification (LFQ) and match-between-runs functions were enabled. The database search results were filtered and exported with a <1% false discovery rate (FDR) at the peptide-spectrum-matched level and the protein level, respectively. Label-free quantification was carried out in MaxQuant using the intensity determination and normalization algorithm as previously described[58]. The "LFQ intensity" of each protein in different samples was calculated as the best estimate, satisfying all of the pairwise peptide comparisons, and this LFQ intensity was almost on the same scale as the summed-up peptide intensities.

A two-sided Student's *t*-test was performed based on protein intensities. Missing values were imputed with a value equal to half of the smallest value in the entire dataset. Proteins meeting the criteria of a fold change greater than 4 or less than 1/4, with a p value <0.05, were considered significantly differentially expressed.

RNA isolation and small RNA sequencing

Total RNA was extracted from immunoprecipitated samples or whole animals of ~100,000 synchronized young adults using TRIzol reagent (Invitrogen, AM9738) following a standard protocol. Small (<200 nt) RNAs were then enriched using the mirVana miRNA Isolation Kit (Ambion, AM1561). In brief, 80 μL of total RNA (<1000 μg) was mixed with 400 μL of mirVana lysis/binding buffer and 48 μL of mirVana homogenate buffer, followed by a 5-min incubation at room temperature. Subsequently, 176 μL of 100% ethanol was added, and the mixture was centrifuged at 2500 × *g* for 4 min at room temperature to pellet large (>200 nt) RNAs. The supernatant containing small (<200 nt) RNAs was transferred to a new tube, and these small RNAs were precipitated with pre-cooled isopropanol at −70 °C. After

centrifugation at 20,000 × *g* at 4 °C for 30 min, the RNA pellet was washed once with 70% pre-cooled ethanol and dissolved in nuclease-free water. About 10 μg of small RNAs were fractionated on a 16% PAGE gel containing 7 M urea, and RNA within the range of 18 nt to 40 nt was excised from the gel. RNA was extracted by soaking the gel in 700 μL of NaCl TE buffer (0.3 M NaCl, 10 mM Tris-HCl, 1 mM EDTA, pH 7.5) overnight. The supernatant was collected through a gel filtration column, and RNA was precipitated with isopropanol, washed with 70% ethanol, and resuspended in 15 μL of nuclease-free water. The RNA samples underwent treatment with RppH (New England Biolabs, M0356S) to convert 22G-RNA 5′ triphosphates to monophosphates. RNA was then concentrated using the RNA Clean and Concentrator-5 Kit (Zymo Research, R1015).

Small RNA libraries were prepared using the NEBNext Multiplex Small RNA Sample Prep Set for Illumina-Library Preparation (New England Biolabs, E7300) according to the manufacturer's protocol. NEBNext Multiplex Oligos for Illumina Index Primers (New England Biolabs, E7335) were used for library preparation. The libraries were sequenced using the Illumina NovaSeq 6000 system.

RNA immunoprecipitation sequencing (RIP-seq)

Approximately 100,000 synchronized young adults were used for RIP-seq. Worms were washed three times with M9 buffer. Worm pellets were resuspended in an equal volume of IP buffer (20 mM Tris-HCl pH 7.5, 150 mM NaCl, 2.5 mM $MgCl_2$, 1 mM dithiothreitol, 0.5% NP-40, 80 U/mL RiboLock RNase Inhibitor (Thermo Scientific, EO0381), 1x protease inhibitor cocktail without EDTA (Promega, G6521)). The pellets were ground in a glass grinder 8–10 times within a 10-min timeframe. Lysates were clarified by centrifugation at 20,000 × *g*, 4 °C, for 15 min. Supernatants were incubated with Anti-Flag Magnetic Beads (MedChemExpress, HY-K0207) at 4 °C for 1.5 h on a rocker. Beads were washed five times with IP wash buffer (20 mM Tris-HCl pH 7.5, 150 mM NaCl, 2.5 mM $MgCl_2$, 1 mM dithiothreitol, 0.5% NP-40), followed by two washes with 1x PBS buffer. Total RNA was extracted using TRIzol reagent (Invitrogen, AM9738) following standard protocols. Small RNA libraries for RNA-seq were prepared as described above and sequenced using an Illumina NovaSeq 6000 system.

Small RNA sequencing data analysis

Fastq reads were trimmed using custom Perl scripts. Subsequently, the trimmed reads were aligned to the *C. elegans* genome build WS230 using Bowtie version 1.3.1[59] with options -v 0 -best -strata. Following alignment, reads ranging from 17 to 40 nucleotides in length were intersected with various genomic features (rRNAs, tRNAs, snoRNAs, miRNAs, piRNAs, protein-coding genes, pseudogenes, and transposons) using BEDTools intersect. Sense and antisense read mappings to specific genomic features were quantified and normalized to reads per million (RPM) by scaling read counts based on total mapped reads, excluding those aligning to structural RNAs (rRNAs, tRNAs, snoRNAs). To account for reads mapping to multiple loci, the read count was adjusted by dividing it by the number of loci where each read perfectly aligned. Specifically, only reads matching the sense annotation without overlap were considered for miRNAs and piRNAs. Reads classified as 22G-RNAs were defined as 21 to 23 nucleotide-long reads with a 5′ G that aligned to protein-coding genes, pseudogenes, or transposons. The resulting RPM values were utilized in downstream analyses, conducted using custom R scripts in R version 4.3.3, leveraging packages including ggplot[60], reshape[61], ggpubr[62], and dplyr[63].

Metagene profiles across gene lengths were generated by analyzing the depth at each genomic position using 21 to 23 nucleotide-long small RNA reads starting with a 5′ G using BEDTools genomecov[64]. Metagene profiles relative to piRNA targeting sites were computed as the mean normalized reads per million at each nucleotide position using the indicated 22G-RNA reads. piRNA targeting sites were identified based on stringent rules for piRNA targeting within the indicated group of transcripts according to previously published guidelines for piRNA target prediction. Groups of genes were then plotted based on the cumulative normalized depth across a 100-nt window around predicted piRNA target sites.

Single molecule fluorescence in situ hybridization (smFISH) and PRG-1 and MUT-16::GFP immunohistochemistry

PolyA or polyUG RNA smFISH was performed on dissected adult gonads. Young adult worms were washed with M9 buffer and transferred onto a glass slide containing Dissection Buffer (1x PBS, 0.1% Tween-20, 0.25 mM levamisole, 1 mM EDTA). Worms were dissected using a 1 mL syringe needle, and then transferred to individual 1.5 mL microcentrifuge tubes. Worms were fixed by incubating with 1 mL of Fix Solution (1x PBS, 3.7% formaldehyde, 0.1% Tween-20) for 30 min at room temperature on a rocker. After fixation, worms were washed once with 1 mL of PBST (1x PBS, 0.1% Tween-20) and then incubated for 10 min with 1 mL of 1x PBS containing 0.1% Triton X-100 at room temperature on a rocker to permeabilize the cells. Following permeabilization, worms were washed twice with 1 mL of PBST, resuspended in 1 mL of 70% ethanol, and incubated at 4 °C for 16–18 h for further processing.

For smFISH combined with immunohistochemistry, dissected worms were washed once with Antibody Wash Buffer (1x PBS, 1 mM EDTA, 0.1% Tween-20) and 50 μL of anti-PRG-1 (custom-made anti-rabbit antibody provided by Dr. Craig Mello lab) or anti-GFP (Santa Cruz, sc-9996) suspended at 1:200 dilution in Antibody Suspension Buffer (1x PBS, 1 mM EDTA, 0.1% Tween-20, 20 mg/mL BSA, 2 mM vanadyl ribonucleoside complex) was added. Samples were shaken at 850 rpm overnight at 4 °C, washed twice with Antibody Wash Buffer, and 50 μL of anti-Rabbit Alexa488 (Jackson Labs, 711-547-003) suspended at a 1:400 dilution in Antibody Suspension Buffer was added. Samples were shaken at 850 rpm for 2 h at room temperature and washed once with Antibody Wash Buffer and once with 2× SSC.

About 1.32 μL of the 2.5 μM polyA or polyUG RNA smFISH probe (Sangon Biotech) was added into fresh HB buffer (297 μL Stellaris RNA FISH hybridization buffer (LGC Biosearch Technologies, SMF-HB1-10) and 33 μL deionized formamide) to prepare a 10 nM polyA RNA smFISH probe hybridization suspension, taking care to protect it from light. The dissected worms were washed with smFISH wash buffer (2x SSC, 10% formamide, 0.1% Tween-20) for 5 min at room temperature on a rocker. After removing excess buffer, 100 μL of the 10 nM polyA RNA smFISH probe suspension was added to each sample, thoroughly mixed, and the samples were incubated for 24 to 36 h at 37 °C, with shaking at 850 rpm in the dark. After completing the probe hybridization, samples were washed once with 1 mL of smFISH wash buffer for 5 min and washed once with 1 mL of 1 μg/mL DAPI in smFISH wash buffer for 30 min in the dark. Then the samples underwent two additional washes with 1 mL of smFISH wash buffer for 5 min each. Excess buffer was carefully removed from the fixed samples. Samples were resuspended in 15 μL of ProLong Gold Antifade Mountant (Invitrogen P36934) and allowed to sit for 30 min. The resuspended gonads were then pipetted onto a microscope slide and covered with a 24 × 24 mm coverslip. Any excess liquid was removed carefully. Nail polish was applied along the edges of the coverslip to prevent drying and movement of the samples during imaging. The slides were cured at room temperature in the dark for approximately 24 h before imaging.

Statistics and reproducibility

Data were expressed as mean values with error bars indicating the standard error mean values in all bar graphs or plots. Statistical significance was evaluated using one-tailed Student's *t*-test or one-way ANOVA, followed by Dunnett's correction for multiple comparisons. GraphPad Prism 8 or R scripts were used for statistical analysis. No statistical method was used to predetermine sample size. No data were excluded from the analyses. The experiments were not randomized. The Investigators were not blinded to allocation during experiments

and outcome assessment. All data for this study were obtained from cultures of *C. elegans* animals at the specified embryonic or adult stages. All imaging experiments were conducted using the indicated number (n) of independent animals. Figure 1a $n = 20$; Fig. 2b $n = 8$ for all genotypes; Fig. 3c $n = 10$ for all genotypes; Fig. 3d $n = 9$ for wild type and $n = 10$ for *npp-24(dz12)*; Fig. 4a $n = 3$; Fig. 4c $n = 4$ for *mip-1*(RNAi) and $n = 6$ for other RNAi treatments; Fig. 4e $n = 8$; Fig. 5e $n = 1$; Fig. 8d $n = 20$ for all genotypes; Fig. 9d $n = 3$.

Reporting summary

Further information on research design is available in the Nature Portfolio Reporting Summary linked to this article.

Data availability

The proteomic data were deposited in the Proteomics Identification database (PRIDE) with the project accession number of PXD051572. The high-throughput sequencing data have been deposited in CNCB via the GSA data repository with accession number CRA016032. Source data are provided with this paper.

Code availability

All custom scripts used for bioinformatic analysis are available in the Supplementary Software, and at GitHub or Zenodo.

References

1. Ghildiyal, M. & Zamore, P. D. Small silencing RNAs: an expanding universe. *Nat. Rev. Genet.* **10**, 94–108 (2009).
2. Brennecke, J. et al. Discrete small RNA-generating loci as master regulators of transposon activity in *Drosophila*. *Cell* **128**, 1089–1103 (2007).
3. Billi, A. C., Freeberg, M. A. & Kim, J. K. piRNAs and siRNAs collaborate in *Caenorhabditis elegans* genome defense. *Genome Biol.* **13**, 164 (2012).
4. Yigit, E. et al. Analysis of the *C. elegans* argonaute family reveals that distinct argonautes act sequentially during RNAi. *Cell* **127**, 747–757 (2006).
5. Lee, H. C. et al. C. elegans piRNAs mediate the genome-wide surveillance of germline transcripts. *Cell* **150**, 78–87 (2012).
6. Shukla, A., Perales, R. & Kennedy, S. piRNAs coordinate poly(UG) tailing to prevent aberrant and perpetual gene silencing. *Curr. Biol.* **31**, 4473–4485.e3 (2021).
7. Ouyang, J. P. T. & Seydoux, G. Nuage condensates: accelerators or circuit breakers for sRNA silencing pathways? *RNA* **28**, 58–66 (2022).
8. Voronina, E., Seydoux, G., Sassone-Corsi, P. & Nagamori, I. RNA granules in germ cells. *Cold Spring Harb. Perspect. Biol.* **3**, a002774–a002774 (2011).
9. Uebel, C. J., Rajeev, S. & Phillips, C. M. *Caenorhabditis elegans* germ granules are present in distinct configurations and assemble in a hierarchical manner. *Development* https://doi.org/10.1242/dev.202284 (2023).
10. Wan, G. et al. Spatiotemporal regulation of liquid-like condensates in epigenetic inheritance. *Nature* **557**, 679–683 (2018).
11. Manage, K. I. et al. A tudor domain protein, SIMR-1, promotes siRNA production at piRNA-targeted mRNAs in C. elegans. *eLife* https://doi.org/10.7554/eLife.56731 (2020).
12. Phillips, C. M., Montgomery, T. A., Breen, P. C. & Ruvkun, G. MUT-16 promotes formation of perinuclear mutator foci required for RNA silencing in the *C. elegans* germline. *Genes Dev.* **26**, 1433–1444 (2012).
13. Chen, X. et al. Germ granule compartments coordinate specialized small RNA production. *Nat. Commun.* **15**, 5799 (2024).
14. Huang, X. et al. Compartmentalized localization of perinuclear proteins within germ granules in *C. elegans*. *Dev. Cell* https://doi.org/10.1016/j.devcel.2024.12.016 (2024).
15. Knaut, H., Pelegri, F., Bohmann, K., Schwarz, H. & Nüsslein-Volhard, C. Zebrafish vasa RNA but not its protein is a component of the germ plasm and segregates asymmetrically before germline specification. *J. Cell Biol.* **149**, 875–888 (2000).
16. Pitt, J. N., Schisa, J. A. & Priess, J. R. P granules in the germ cells of *Caenorhabditis elegans* adults are associated with clusters of nuclear pores and contain RNA. *Dev. Biol.* **219**, 315–333 (2000).
17. Lim, A. K. & Kai, T. Unique germ-line organelle, nuage, functions to repress selfish genetic elements in *Drosophila melanogaster*. *Proc. Natl Acad. Sci. USA* **104**, 6714–6719 (2007).
18. Chuma, S., Hosokawa, M., Tanaka, T. & Nakatsuji, N. Ultrastructural characterization of spermatogenesis and its evolutionary conservation in the germline: germinal granules in mammals. *Mol. Cell. Endocrinol.* **306**, 17–23 (2009).
19. Updike, D. L., Hachey, S. J., Kreher, J. & Strome, S. P granules extend the nuclear pore complex environment in the *C. elegans* germ line. *J. Cell Biol.* **192**, 939–948 (2011).
20. Sheth, U., Pitt, J., Dennis, S. & Priess, J. R. Perinuclear P granules are the principal sites of mRNA export in adult *C. elegans* germ cells. *Development* **137**, 1305–1314 (2010).
21. Chemes, H. E., Fawcett, D. W. & Dym, M. Unusual features of the nuclear envelope in human spermatogenic cells. *Anat. Rec.* **192**, 493–511 (1978).
22. Fawcett, D. W. & Chemes, H. E. Changes in distribution of nuclear pores during differentiation of the male germ cells. *Tissue Cell* **11**, 147–162 (1979).
23. Updike, D. L. & Strome, S. A genomewide RNAi screen for genes that affect the stability, distribution and function of P granules in *Caenorhabditis elegans*. *Genetics* **183**, 1397–1419 (2009).
24. Voronina, E. & Seydoux, G. The *C. elegans* homolog of nucleoporin Nup98 is required for the integrity and function of germline P granules. *Development* **137**, 1441–1450 (2010).
25. Uebel, C. J., Agbede, D., Wallis, D. C. & Phillips, C. M. Mutator foci are regulated by developmental stage, RNA, and the germline cell cycle in *Caenorhabditis elegans*. *G3* **10**, 3719–3728 (2020).
26. Lev, I. et al. Germ granules govern small RNA inheritance. *Curr. Biol.* https://doi.org/10.1016/j.cub.2019.07.054 (2019).
27. Brown, J., Zhang, D., Gaylord, O., Chen, W. & Lee, H.-C. Sensitized piRNA reporter identifies multiple RNA processing factors involved in piRNA-mediated gene silencing. *Genetics* https://doi.org/10.1093/genetics/iyad095 (2023).
28. Du, Z. et al. Condensate cooperativity underlies transgenerational gene silencing. *Cell Rep.* **42**, 112859 (2023).
29. Cordeiro Rodrigues, R. J. et al. PETISCO is a novel protein complex required for 21U RNA biogenesis and embryonic viability. *Genes Dev.* **33**, 857–870 (2019).
30. Belicard, T., Jareosettasin, P. & Sarkies, P. The piRNA pathway responds to environmental signals to establish intergenerational adaptation to stress. *BMC Biol.* **16**, 103 (2018).
31. Cohen-Fix, O. & Askjaer, P. Cell biology of the *Caenorhabditis elegans* nucleus. *Genetics* **205**, 25–59 (2017).
32. Shirayama, M. et al. PiRNAs initiate an epigenetic memory of nonself RNA in the *C. elegans* germline. *Cell* **150**, 65–77 (2012).
33. Ashe, A. et al. PiRNAs can trigger a multigenerational epigenetic memory in the germline of *C. elegans*. *Cell* **150**, 88–99 (2012).
34. Chen, W. et al. GLH/VASA helicases promote germ granule formation to ensure the fidelity of piRNA-mediated transcriptome surveillance. *Nat. Commun.* **13**, 5306 (2022).
35. Price, I. F., Wagner, J. A., Pastore, B., Hertz, H. L. & Tang, W. *C. elegans* germ granules sculpt both germline and somatic RNAome. *Nat. Commun.* **14**, 5965 (2023).
36. Bley, C. J. et al. Architecture of the cytoplasmic face of the nuclear pore. *Science* **376**, eabm9129 (2022).

37. Fontana, P. et al. Structure of cytoplasmic ring of nuclear pore complex by integrative cryo-EM and AlphaFold. *Science* **376**, eabm9326 (2022).
38. Cipriani, P. G. et al. Novel LOTUS-domain proteins are organizational hubs that recruit *C. elegans* vasa to germ granules. *eLife* https://doi.org/10.7554/eLife.60833 (2021).
39. Price, I. F., Hertz, H. L., Pastore, B., Wagner, J. & Tang, W. Proximity labeling identifies LOTUS domain proteins that promote the formation of perinuclear germ granules in *C. elegans*. *eLife* **10**, e72276 (2021).
40. Quarato, P. et al. Germline inherited small RNAs facilitate the clearance of untranslated maternal mRNAs in *C. elegans* embryos. *Nat. Commun.* **12**, 1441 (2021).
41. Shen, E.-Z. et al. Identification of piRNA binding sites reveals the argonaute regulatory landscape of the *C. elegans* germline. *Cell* **172**, 937–951.e18 (2018).
42. Zhang, D. et al. The piRNA targeting rules and the resistance to piRNA silencing in endogenous genes. *Science* **359**, 587–592 (2018).
43. Gu, W. et al. Distinct argonaute-mediated 22G-RNA pathways direct genome surveillance in the *C. elegans* germline. *Mol. Cell* **36**, 231–244 (2009).
44. Claycomb, J. M. et al. The argonaute CSR-1 and its 22G-RNA cofactors are required for holocentric chromosome segregation. *Cell* **139**, 123–134 (2009).
45. Wu, W.-S. et al. piRTarBase: a database of piRNA targeting sites and their roles in gene regulation. *Nucleic Acids Res.* **47**, D181–D187 (2019).
46. Wedeles, C. J. et al. Protection of germline gene expression by the *C. elegans* argonaute CSR-1. *Dev. Cell* **27**, 664–671 (2013).
47. Wu, W.-S. et al. Transcriptome-wide analyses of piRNA binding sites suggest distinct mechanisms regulate piRNA binding and silencing in C. elegans. *RNA* **29**, 557–569 (2023).
48. Cornes, E. et al. piRNAs initiate transcriptional silencing of spermatogenic genes during C. elegans germline development. *Dev. Cell* **57**, 180–196.e7 (2022).
49. Frey, S., Richter, R. P. & Gorlich, D. FG-rich repeats of nuclear pore proteins form a three-dimensional meshwork with hydrogel-like properties. *Science* **314**, 815–817 (2006).
50. Tsai, H.-Y. et al. A ribonuclease coordinates siRNA amplification and mRNA cleavage during RNAi. *Cell* **160**, 407–419 (2015).
51. Shukla, A. et al. poly(UG)-tailed RNAs in genome protection and epigenetic inheritance. *Nature* https://doi.org/10.1038/s41586-020-2323-8 (2020).
52. Zhao, C. et al. HERD-1 mediates multiphase condensate immiscibility to regulate small RNA-driven transgenerational epigenetic inheritance. *Nat. Cell Biol.* **26**, 1958–1970 (2024).
53. Jadhav, S., Rana, M. & Subramaniam, K. Multiple maternal proteins coordinate to restrict the translation of *C. elegans nanos-2* to primordial germ cells. *Development* **135**, 1803–1812 (2008).
54. Ouyang, J. P. T., Zhang, W. L. & Seydoux, G. The conserved helicase ZNFX-1 memorializes silenced RNAs in perinuclear condensates. *Nat. Cell Biol.* **24**, 1129–1140 (2022).
55. Xu, F. et al. A cytoplasmic argonaute protein promotes the inheritance of RNAi. *Cell Rep.* **23**, 2482–2494 (2018).
56. Folkmann, A. W., Putnam, A., Lee, C. F. & Seydoux, G. Regulation of biomolecular condensates by interfacial protein clusters. *Science* **373**, 1218–1224 (2021).
57. Seroussi, U. et al. A comprehensive survey of C. elegans argonaute proteins reveals organism-wide gene regulatory networks and functions. *eLife* https://doi.org/10.7554/eLife.83853 (2023).
58. Cox, J. et al. Accurate proteome-wide label-free quantification by delayed normalization and maximal peptide ratio extraction, termed MaxLFQ. *Mol. Cell. Proteom.* **13**, 2513–2526 (2014).
59. Langmead, B., Trapnell, C., Pop, M. & Salzberg, S. L. Ultrafast and memory-efficient alignment of short DNA sequences to the human genome. *Genome Biol.* https://doi.org/10.1186/gb-2009-10-3-r25 (2009).
60. Wickham, H. *ggplot2: Elegant Graphics for Data Analysis* (Springer-Verlag, 2016).
61. Wickham, H. Reshaping data with the {reshape} package. *J. Stat. Softw.* **21**, 1–20 (2007).
62. Kassambara, A. ggpubr: "ggplot2" based publication ready plots. (2020).
63. Wickham, H., François, R., Henry, L. & Müller, K. dplyr: a grammar of data manipulation (2021).
64. Quinlan, A. R. & Hall, I. M. BEDTools: a flexible suite of utilities for comparing genomic features. *Bioinformatics* **26**, 841–842 (2010).

Acknowledgements

Some strains used in this study were provided by the CGC, which is funded by the NIH Office of Research Infrastructure Programs (P40 OD010440). This work is supported in part by NIH grant R01-GM132457 to H.-C.L.; the National Natural Science Foundation of China (grants 31922019) and the program for HUST Academic Frontier Youth Team (grant 2018QYTD11) to D.Z.

Author contributions

Conceptualization, supervision, funding acquisition, and writing: D.Z. and H.-C.L., Investigation: K.S., Y.Z., Z.D., S.C.L., I.L., X.F., and D.Z., Data analyses: D.Z. and K.S., Bioinformatics analyses: D.Z.

Competing interests

The authors declare no competing interests.

Additional information

Supplementary information The online version contains supplementary material available at https://doi.org/10.1038/s41467-025-59526-3.

Correspondence and requests for materials should be addressed to Heng-Chi Lee or Donglei Zhang.

Peer review information *Nature Communications* thanks the anonymous reviewers for their contribution to the peer review of this work. A peer review file is available.

Reprints and permissions information is available at http://www.nature.com/reprints

Publisher's note Springer Nature remains neutral with regard to jurisdictional claims in published maps and institutional affiliations.

Open Access This article is licensed under a Creative Commons Attribution-NonCommercial-NoDerivatives 4.0 International License, which permits any non-commercial use, sharing, distribution and reproduction in any medium or format, as long as you give appropriate credit to the original author(s) and the source, provide a link to the Creative Commons licence, and indicate if you modified the licensed material. You do not have permission under this licence to share adapted material derived from this article or parts of it. The images or other third party material in this article are included in the article's Creative Commons licence, unless indicated otherwise in a credit line to the material. If material is not included in the article's Creative Commons licence and your intended use is not permitted by statutory regulation or exceeds the permitted use, you will need to obtain permission directly from the copyright holder. To view a copy of this licence, visit http://creativecommons.org/licenses/by-nc-nd/4.0/.

© The Author(s) 2025